# Modelling the propagation of polar cap patches

Sean William Bråthen
Assosciate professor: Lasse B. N. Clausen
Co-supervisor: Dr. Anna K. F. Follestad


Thesis submitted for the degree of
Master in Space Physics and Technology
60 credits

Department of Physics
Faculty of mathematics and natural sciences

UNIVERSITY OF OSLO

Spring 2021

# Modelling the propagation of polar cap patches

Sean William Bråthen
Assosciate professor: Lasse B. N. Clausen
Co-supervisor: Dr. Anna K. F. Follestad

Modelling the propagation of polar cap patches

http://www.duo.uio.no/

Printed: Reprosentralen

# Acknowdelgments

The authors acknowledge the use of SuperDARN data. SuperDARN is a collection of radars funded by national scientific funding agencies of Australia, Canada, China, France, Italy, Japan, Norway, South Africa, United Kingdom and the United States of America.

First I would like to thank my main supervisor, Lasse B. N. Claussen, for his guidance and motivation. I am grateful for the new insight on space weather research that he has given me. I would also like thank my co-supervisor, Anna K. F. Follestad, for helping me at the start of my thesis. I wish her the best of luck on her new ventures.

A big thanks to Bjørn Lybekk for supplying me with a computer and the 4DSpace Strategic Research Initiative for providing me with an office that was of grate use when accessible. I also want to give thanks to the library of the University of Oslo's for allowing me to access any research article that they have at their disposal.

Last but not least I would like to thank friends and family for their support, and a special thanks to the group of co-master students: Aksel Graneng, Amund Fredriksen, Lise Nguyen, Michael S Bitney & Saida Ve. I could not ask for a more helpful and friendly group of co-students.

This thesis would not have been possible without the help of anyone mentioned.

# Abstract

Space weather explores dynamics between the Sun- interplanetary medium and the Earth's magnetosphere and upper atmosphere. Space weather is known for causing disturbances in Global Navigation Satellite Systems (GNSS) and these disturbances are rapid changes in the amplitude and phase of a signal that a receiver receives, known as scintillations. This reduces accuracy in GNSS based technology. Just like terrestrial weather, space weather can not be controlled, but with a sufficiently good forecasting model we can predict and prepare for the weather that is to come. In 1961 it was suggested by Dungey that interplanetary magnetic field (IMF) carried by the plasma in the solar wind would interact with the Earth's magnetosphere, through magnetic reconnection. A southward facing IMF can magnetically reconnect at the dayside, causing magnetospheric convection. During this process the plasma located in the ionosphere would get carried by the convecting magnetic field, causing areas of higher density plasma to occur at the dayside ionosphere.These areas of high-density plasmas are called polar cap patches when propagating through the polar cap. When these patches exit at the auroral oval, they form plasma blobs. These blob structures are known to cause significant scintillations and it is therefore interesting to predict when and where these blobs occur.

This paper aims to determine whether the Expanding/Contracting Polar Cap (ECPC) paradigm can be used as a basis for such a forecasting model. The model calculates the convection. We use this convection to calculate the E×B-drift, from the changing polar cap flux that the polar cap patches would drift with. We place tracer particles along the dayside OCB to study the propagation of a polar cap patch. We observe that the model produces different propagation in response to different time series of reconnection rates. We estimate that the dynamics not included in the model has varying effects on accuracy in propagation prediction. This include flow channels, that we estimate reduce propagation time by 10 minutes if we assume mean drift velocity to be 400m/s. As for the assumption of a symmetrical twin-cell convection pattern, we determine this to make for larger uncertainties. A tracer particle would have smaller uncertainties in propagation times if it started closer to noon, but closer to dawn/dusk would lead to more uncertainties and odd behaviour in the model.

# Contents


**1 Introduction** **5**

**2 Theory** **7**

2.1 A short introduction to space weather . . . . . 7

2.2 Solar wind-magnetosphere interaction . . . . . 8

2.2.1 Magnetic reconnection and the Dungey cycle . . . . . 9

2.2.2 Twin-cell convection . . . . . 11

2.2.3 Polar cap patches and scintillations . . . . . 12

**3 Methodology** **14**

3.1 Convection model . . . . . 14

3.1.1 Prediction model (ECPC) . . . . . 14

3.1.2 Tracing the plasma convection . . . . . 23

3.1.3 Proof of concept . . . . . 26

**4 Results** **28**

4.1 Case A: assuming reconnection time series similar to previous case study 29

4.2 Case B: IMF Z interval -0.5nT turning to 0.5nT . . . . . 34

4.3 Case C: IMF Z interval -2.0nT turning to 2.0nT . . . . . 39

4.4 Case D: IMF Z interval -5.0nT turning to 5.0nT . . . . . 44

4.5 Case E: IMF Z interval turning from strong to weak . . . . . 49

4.6 Case F: IMF Z interval -0.5nT turning to 0.5nT with an offset to the generated values . . . . . 54
4.7 Case G: IMF Z interval -5.0nT turning to 5.0nT with an offset to the generated values . . . . . 59
4.8 Propagation time distribution . . . . . 63

**5 Discussion** **66**
5.1 Predicted convection and real life cases . . . . . 66
5.2 Polar cap flux, electric fields and mean velocities . . . . . 68
5.3 Tracer paths and propagation time distribution . . . . . 69

**6 Conclusion** **72**

**7 Outlook** **73**

**References** **74**

# Chapter 1

# Introduction

Space weather is a branch space physics. The study of space weather includes the study natural phenomena occurring between the Sun and the Earth's magnetosphere, ionosphere and thermosphere (Prölss, 2012). It has been known to cause problems for technology at all altitudes. This includes technology that is at higher altitudes, such Global Navigation Satellite Systems (GNSS), mid-altitudes, such as aviation, and low-altitudes such as power grids. Some examples of space weather affecting our daily lives: On march 13-14 1989, a large magnetic storm would send electric currents surging through power grids located at high-latitude, leading the citizens of Quebec power-less for more than 9 hours (Allen, Sauer, Frank & Reiff, 1989; Nagatsuma, Kataoka & Kunitake, 2015). In the period 2000 to 2005 there have been seventeen severe magnetic storms where, during all these events, there was reported anomalies in the signalling system for Russian railway located at latitudes 58 to 60 degrees north (Eroshenko et al., 2010).

The effect of space weather on Global Navigation Satellite Systems (GNSS) has been of great interest and its effects are well documented (Jakowski, Wilken, Schlueter, Stankov & Heise, 2005; Jakowski, Stankov & Klaehn, 2005; Sreeja, 2016). GNSS technology is widely used by both consumers and industries and thus reliability of this system is of high demand. When GNSS signals propagate through the ionosphere the signals may experience change in their phase and amplitude (Yeh & Liu, 1982; Kintner, Ledvina & De Paula, 2007), known as scintillations. Some of the earliest sightings date back to 1940s (Hey, Parsons & Phillips, 1946). Scintillations reduce the accuracy in GNSS technology and may even cause loss of lock (Garner et al., 2011; Jacobsen & Andalsvik, 2016). Some of the largest disturbances in GNSS signals, due to scintillations, occur when a plasma patch propagates through the polar cap and exits through the polar cap nightside (Moen et al., 2013; Jin, Moen & Miloch, 2014). For this reason it is of great interest to study and predict the nightside arrival of

aforementioned patches.

Islands of elevated plasma densities can propagate into the polar cap at the dayside, due to convection. The convection is driven by dayside and nightside reconnection (Cowley & Lockwood, 1992, 1992). When crossing the dayside Open-Closed Boundary and into the polar cap these islands of elevated plasma densities become known as polar cap patches. they are high-density plasma clouds (Crowley et al., 2000). These regions are only labelled as patches while inside the polar cap and blobs when outside (Crowley et al., 2000). They appear at the dayside and there are several interpretations as to how (Lockwood & Carlson Jr, 1992; Moen et al., 2006). These patches may then propagate antisunward along with ionospheric convection pattern and exit through the auroral oval where they form a blob (Crowley et al., 2000), these shapes are associated with large phase and amplitude scintillations (Weber et al., 1985).

In order to study the propagation of patches across the polar cap, one needs to have information about the movement of plasma.The Expanding/Contracting Polar Cap paradigm (ECPC) provides us with a description of the convection pattern, that transports the patches from the reservoir and across the polar cap. This process is driven by dayside and nightside reconnection (Cowley & Lockwood, 1992; Lockwood & Cowley, 1992). In a case study by Follestad et al. (2019), they used the dayside and nightside reconnection rates as arguments for the ECPC model. These reconnection rates were calculated from polar cap potential, this data was collected from the Super Dual Auroral radar network (SuperDARN) website. They assumed that the polar cap potential is the average of the two reconnection rates. In their case study the ECPC would predict the arrival of the patch at the auroral over with a 5 minute accuracy (Follestad, Clausen, Thomas, Jin & Coster, 2019), a promising result.

Being able to predict the arrival of patches could help predict scintillations, being of great benefit of industries and consumers who rely on the precise nature of GNSS. A well developed space weather forecasting system could save users time and money. The goal for this thesis will be to further study the ECPC model as a model to be used in space weather forecasting, determining its accuracy through the use of synthetically generated reconnection rates and study polar cap patch propagation as presented by the model.

# Chapter 2

# Theory

In this chapter will provide a theoretical background to better understand how space weather affect Global Navigation Satellite Systems (GNSS). First we introduce the concept of space weather, before explaining how solar wind interacts with the Earth's magnetic fields. Then we will go on to explain a more concrete space weather phenomena, polar cap patches and how this affects us.

## 2.1 A short introduction to space weather

Space weather refers to the dynamics of a large coupled system, that of the Sun, interplanetary medium and the Earth's magnetosphere and upper atmosphere (Russell, Luhmann & Strangeway, 2016). There is a huge interest in studying space weather, because it is known to affect technology on a large scale and understanding the underlying physics is important. The constant stream of particles from the Sun is what drives space weather. The solar wind comes from the Sun, which is very hot. It consists of charged ions and electrons and is very hot, making te solar wind a plasma. Due to the large conductivity of the solar wind the frozen-in theorem applies (Pécseli, 2013). It states that plasma and magnetic fields are frozen together and will therefore propagate together. This is illustrated in Figure 2.1, where we see magnetic field lines being carried away by plasma.

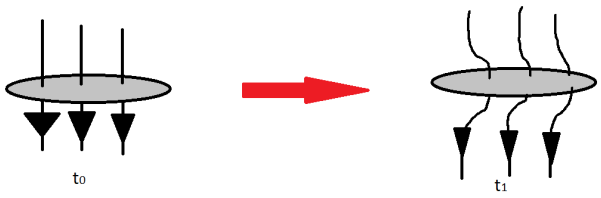


Figure 2.1: An enclosed area of plasma with high conductivity penetrates magnetic field lines at time $t_0$ and become frozen together. After a time $t_1$ they propagate in the same direction.

It has been established that the solar wind consist of plasma and magnetic fields. This plasma carries with it the solar magnetic fields with it, known as the interplanetary magnetic field (IMF). The IMF enable solar wind to interact with the Earth's magnetosphere.

## 2.2 Solar wind-magnetosphere interaction

The Earth is approximated as a dipole. The magnetic field is directed from the south pole and towards the north pole, each pole located by their respective geographical pole. The area in which these magnetic field lines dominate is what is known as the Earth's magnetosphere. It will act as an obstacle to any incoming IMF, but their interaction distort the magnetic field of Earth. This dipole distortion can be seen in Figure 2.2. Here we are able to see how the magnetosphere is compressed at the dayside and elongated at the nightside, due to the interaction wit the IMF. The magnetopause can also be seen, the boundary separating the IMF from the region where Earth's magnetic field dominates. An IMF has a z-component, this component is parallel to the north pole - south pole axis of the Earth. We say that an IMF is directed southward if the z-component is anti-parallel to that of the Earth's and northward if it is parallel.This is illustrated by red and blue field lines respectively in Figure 2.2.

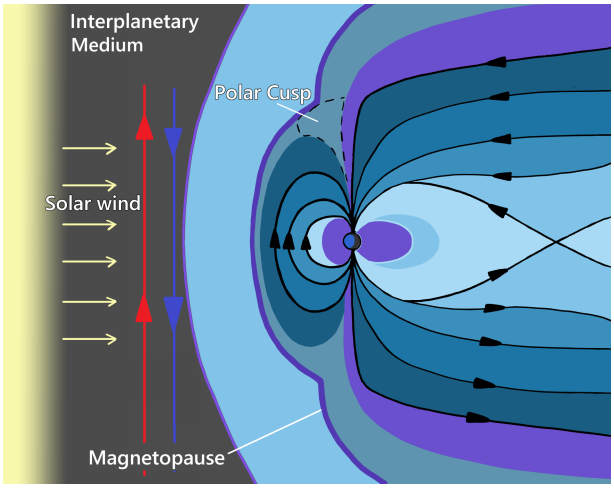


Figure 2.2: This figure illustrates how the Earth's magnetosphere as a distorted dipole. A northward facing IMF (Bz $>$ 0) is illustrated by the red line and a southward facing IMF (Bz $<$ 0) is illustrated by the blue line. Here the magnetopause is also present, acting as a boundary between the magnetosphere and the solar wind. Illustration is based on an illustration presented by Russel et al.(2016).

### 2.2.1 Magnetic reconnection and the Dungey cycle

The process where two magnetic field lines couple together is known as magnetic reconnection. Two opposite directed magnetic field lines decouple and connect with each other, given that they are substantially close to each other. This process is seen in Figure 2.3, panel a) shows an incoming IMF (blue), propagating towards the magnetic field in the magnetosphere (black). The orientation of the Earth's magnetic field line is northward and if the IMF is directed southward the two will reconnect as seen in panel b.

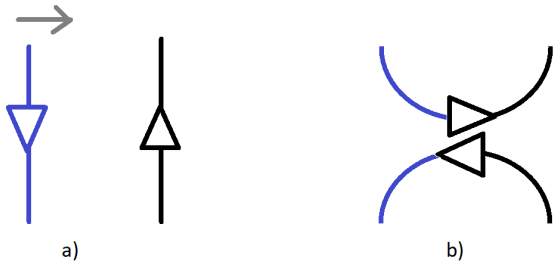


Figure 2.3: Event *a* illustrates how a southward IMF transported by the solar wind (blue) propagates towards the magnetic field lines of Earth (black). While event *b* illustrates the new magnetic field after reconnection, combining the two magnetic field lines into two new.

As mentioned above, if an incoming IMF has southward facing component, relative to the pole-axis of earth, then magnetic reconnection can occur at the dayside by the magnetopause. This allows the plasma in the solar wind to enter the magnetosphere and this reconnection also leads to the magnetic open flux being transported from the dayside to the nightside of the Earth, an antisunwards flow. This process of flux transportation triggers a nightside reconnection by the magneto tail and a returning flow to the dayside. This is known as the Dungey cycle, named after Dungey (1961) who was the first to understand how reconnection could lead to this momentum transfer from the solar wind to the magnetosphere. This cycle is presented in Figure 2.4, it is a illustration presented by Jackmann et al. (2014) (therein courtesy of Steve Milan). The order of the cycle, describing the antisunward flow and sunward return, is denoted by ascending numbers 1 tough 7. The open magnetic flux (we will refer to it as the polar cap flux from now on) is the magnetic field flux between the IMF and magnetosphere . The lack of a field line closing at the Earth itself is seen clearly at points 2 and 3 in the figure.

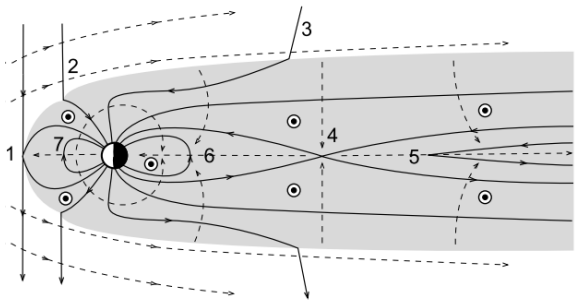


Figure 2.4: A diagram explaining the Dungey cycle, starting with dayside reconnection and ending at the return of flow back into the Earth dayside. The cycle is ordered in ascending numbers 1-7, Jackmann et al. (2014).

### 2.2.2 Twin-cell convection

The magnetospheric convection is driven by magnetic reconnection and due to the frozen-in theorem the plasma in the ionosphere will be carried along with this convection. The resulting plasma motion is what is known as a twin-cell pattern, this convection pattern is illustrated in Figure 2.5. The plasma will convect, crossing the Polar Cap Boundary/Open-Closed Boundary (we will refer to it as OCB), and then antisunwards into the polar cap, before exiting the polar cap at the nightside OCB and into the return flow region.

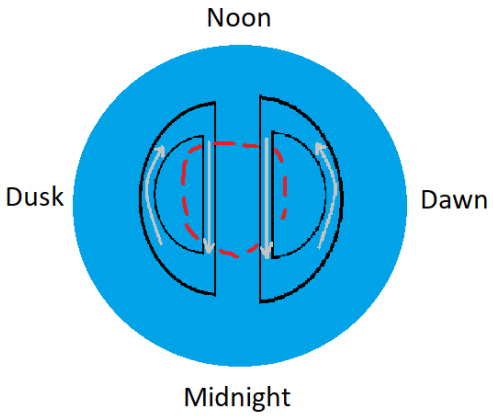


Figure 2.5: An illustration of the ionospheric convection pattern, a twin-cell convection pattern at the northern hemisphere, resulting from the Dungey cycle. The red stapled line represents the polar cap.

The illustration is that of a perfect twin-cell convection pattern. Studies by Pettigrew et al. (2010) show that these convection patterns are neither symmetrical around the noon-midnight axis nor are they guaranteed to be the same size. Changes in the polar cap flux induces an electric field that is directed from dawn to dusk, this is due to the Dungey cycle. Plasma entering the polar cap will experience a E×B-drift due to this electric field (Siscoe & Huang, 1985) and the Earth's magnetic field. The drift speed has been observed to typically be in the range 300-1000m/s (Weber et al., 1984).

### 2.2.3 Polar cap patches and scintillations

The increase of plasma density in the polar cap appear as clouds of high-density plasma, known as polar cap patches (Weber et al., 1984). The formation and transportation of these patches are driven by the solar wind - magnetosphere interaction. Dayside reconnection increases the polar cap flux, leading to magnetospheric convection and the ionospheric plasma is carried with this convection causing clouds of high-density plasma to enter the polar cap. Once these clouds enter the polar cap they become known as polar cap patches. They convect antisunwards, exiting through the auroral oval and returns through the return flow region. This motion is known as a twin-cell convection. Propagation times, from entering the polar cap until exiting, is observed to be between 2 and 3 hours (Oksavik, Barth, Moen & Lester, 2010). When exiting the polar cap at the auroral oval the patch will clump up and turn into a blob (Crowley et al., 2000). These blob structures are associated with large disturbances due to scintillations (Weber et al., 1985).

Signal disturbances due to rapid changes in their phase and amplitude are known as scintillations (Yeh & Liu, 1982; Kintner et al., 2007). These disturbances reduce accuracy in GNSS based technology and can even cause loss of lock (Garner et al., 2011; Jacobsen & Andalsvik, 2016). Refraction and diffraction is the underlying mechanism of this phenomena (McCaffrey & Jayachandran, 2019). The refractive index of the ionosphere is not uniform, it depends on the frequency of the incoming wave and the electron density in the path of the signal. The refractive index not constant due to irregularities in the plasma density of the ionosphere, causing unpredictable phase shifts in the signals. Phase shift in the incoming signals lead to constructive and destructive interference, changing the amplitude of the signal. Figure 2.6 illustrates how a signal, sent from a satellite, is disturbed due to scintillations, and unrecognisable when the signal arrives at the receiver.

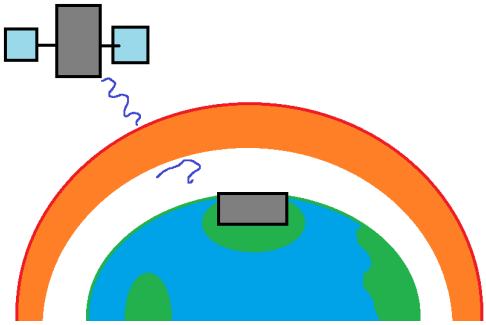

Figure 2.6: In the upper left a satellite sends a plane wave towards a ground based receiver, sending it through the ionosphere coloured orange. By the time of arrival the signal is unrecognisable due to both destructive and constructive interference.

# Chapter 3

# Methodology

In this chapter we explain the methodology for the model we use. First we explain the prediction model in use, known as the Expanding/Contracting Polar Cap paradigm (abbreviated as ECPC) (Lockwood & Cowley, 1992). This is a convection model where plasma patches are transported from dayside the dayside reservoir to the nightside Open-Closed Boundary (also known as the auroral oval). First we will go through the model and equations necessary to describe the model. Later we will compare our model for certain parameters given by Milan (2013) to ensure that our model can reproduce the same results. We want to study the behaviour of plasma patches and how they propagate for different cases. To study this further we introduce tracer particles to the model and observe their behaviour for different cases and different starting positions.

## 3.1 Convection model

### 3.1.1 Prediction model (ECPC)

In the model presented by *Milan* (2013), the electric field **E**, associated with the propagating plasma convection, can be expressed by the electrostatic potential $\Phi$. By observing time scales larger than a couple of 10 s, we can assume that the ionosphere located magnetic field to be stationary (Milan, 2013). This has an implication on Faraday's law shown in equation 3.1

$$\nabla \times E = -\frac{\partial B}{\partial t} = 0 \tag{3.1}$$

The consequence of this assumption implies by Faraday's law that the electric field $E$ related to the moving plasma convection is irrotational. Thus we obtain the following equation:

$$\mathbf{E} = -\nabla\Phi \tag{3.2}$$

The model in use has been developed by (Siscoe & Huang, 1985), (Freeman & Southwood, 1988), (Freeman, 2003) and (S. Milan, Gosling & Hubert, 2012).

The convection model separates the polar ionosphere into three regions. The three regions are the polar cap, return flow region and a low-latitude region. In the three region we observe antisunward plasma drift, domination of sunward plasma drift and no convective motion respectively. The boundaries between these regions are where significant gradients in the conductivities are expected to occur (S. E. Milan, 2013). Region 1 currents form a ring at the polar cap boundary or open/closed (OCB) field boundary. The region 2 currents form a ring at the low-latitude boundary of the convection pattern [Milan, 2013]. It is assumed that both rings are sufficiently thin so that their latitudinal extent can be neglected, this applies to both rings. The northern hemisphere can be mapped out by the use of spherical coordinates, the earth's radii, magnetic local time (MLT) as longitude $\theta$ and colatitude $\lambda$. $\theta = 0$ is defined midnight in magnetic local time (00 MLT) and $\theta = \pi/2$, $\theta = \pi$, $\theta = 3\pi/2$ is defined as 06-, 12-, and 18 MLT respectively. Motion in this coordinate system is positive for increasing MLT and equatorwards motion respectively. An illustration is seen in Figure 3.1

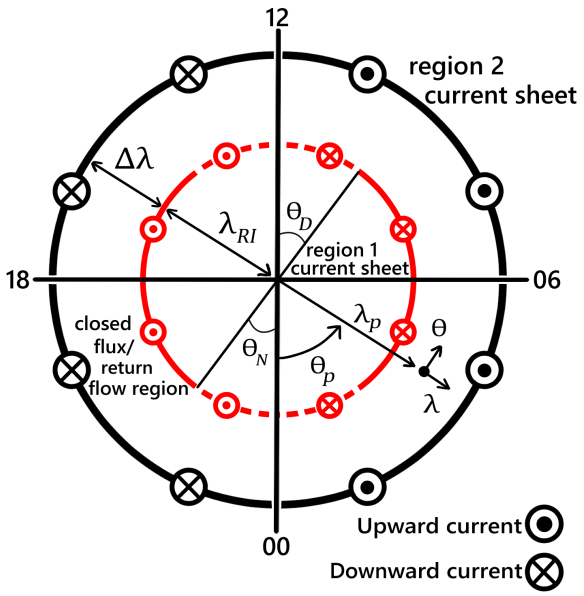


Figure 3.1: This figure display main features for our model. The region 1 and region 2 are displayed as a red- and black circle respectively, centred at the geomagnetic pole. The region 1 currents are located at colatitude $\lambda_{R1}$ while the region 2 currents are located at the colatitude $\lambda_{R2} = \lambda_{R1} + \Delta\lambda$.They are also located at the same location as the open/closed field line boundary and the Heppner-Maynard boundary. The day- and nightside merging gaps are displayed by the dashed lines and the day-/nightside throat shown as $\theta_D$ and $\theta_N$. Illustration based on model by *Milan* [2013].

The complete spherical description can be seen in Figure 3.2, where the latitudes 60, 70 and 80 are visualized. In our model we will be calculating for latitudes 60-90. degrees for the northern hemisphere.

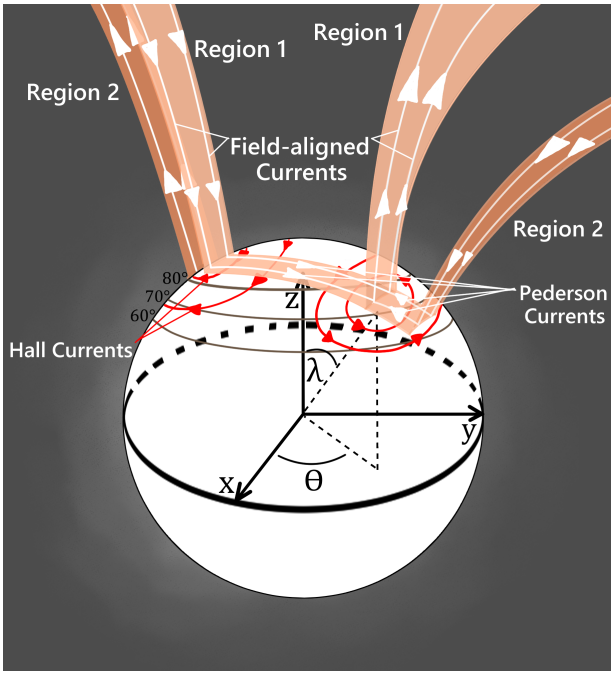


Figure 3.2: The figure displays a three dimensional view of the earth model described earlier. Field aligned, Pedersen, Hall, region 1 and region 2 currents are all visualized.

Another assumption that will further simplify the expression for currents flowing parallel to the magnetic field is that we assume the conductivity to be uniform for both the polar cap region and the return flow region [Milan, 2013]. now assuming that the Birkeland currents are confined to the three regions and a spatially uniform conductivity within the domain we get that the following expression [Milan, 2013]

$$\nabla^2 \Phi = 0 \tag{3.3}$$

Next, by assuming that the ionosphere is a thin, spherical sheet, then (3.3) has two arguments, colatitude $\lambda$ and magnetic azimuth $\theta$ [Milan, 2013]. The electrostatic potential and the electric field can represented with the longitude and colatitude as arguments so that $\Phi(\theta, \lambda)$ and $\mathbf{E}\ (\theta, \lambda) = E_\theta\ \hat{\theta} + E_\lambda\ \hat{\lambda}$. where $\hat{\theta}$ and $\hat{\lambda}$ are positive for increasing MLT and equatorwards motion respectively.

The earth has a magnetic field that is viewed as a distorted magnetic dipole, but when only considering high-latitudes we we can model the magnetic field as a dipole with only a radial magnetic component. The expression for the radial component of the Earth's magnetic field, assuming it is a dipole, is given by

$$B_r(\lambda) = 2B_{eq}\cos\lambda \tag{3.4}$$

The polar cap flux is equal to radial component of the magnetic field integrated over the area of the polar cap. We assume the polar cap til be circular and for the centre to be located at the geomagnetic pole. We also assume that the region 1 currents, that form a circular boundary, is located at the same location as the open/closed field line boundary [Milan, 2013]. This is at the colatitude position $\lambda_{R1}$.

$$F_{PC} = 2\pi R_E^2 B_{eq}\sin^2\lambda_{R1} \tag{3.5}$$

This allows us to locate the open/closed field line boundary for a given magnetic flux. The boundary is located at the colatitude of region 1 $\lambda_{R1}$

$$\lambda_{R1} = \arcsin\left(\frac{F_{PC}}{2\pi R_E^2 B_{eq}}\right) \tag{3.6}$$

With a changing magnetic flux there is also a change in the OCB location. This can therefore be found by calculating $\lambda_{R1}$ as a function of the changing magnetic flux. The change in magnetic flux is described by Milan (2013) as

$$\frac{dF_{PC}}{dt} = \Phi_D - \Phi_N \tag{3.7}$$

Equation 3.7 shows how the dayside reconnection rate is related to the polar cap flux via Faraday's law (Siscoe & Huang, 1985).

A changing $\lambda_{R1}$ implies that the OCB and region 1 currents are moving with oval speed positive equatorwards

$$V_{R1} = R_E\frac{d\lambda_{R1}}{dt} = \frac{(\Phi_D - \Phi_N)}{2\pi R_E^2 B_{eq}\sin 2\lambda_{R1}} \tag{3.8}$$

The dayside merging gap has an angular half-widths of $\theta_D$ centered at $\theta = \pi$ and the nightside merging gap has an angular half-width og $\theta_N$ centred at $\theta = 0$ [Milan, 2013]. The lengths of these gaps are given by $l_D = 2\theta_D R_E sin\lambda_{R1}$ and $l_N = 2\theta_N R_E sin\lambda_{R1}$ respectively (S. E. Milan, 2013)

The ionospheric current flow is considered to be perpendicular to the open/closed field line boundary at all latitudes (S. E. Milan, 2013) so the electric field perpendicular to the boundary is just 0.

$$E_\lambda(\lambda_{R1}, \theta) = 0 \tag{3.9}$$

From $\mathbf{E}$ = - $\mathbf{V} \times \mathbf{B}$, we can calculate the parallel electric field component at the OCB for the portions where there is no reconnection (S. E. Milan, 2013)

$$E_\theta(\lambda_{R1}, \theta) = E_B = -V_{R1} B_r, \theta_N < |\theta| < \pi - \theta_D \tag{3.10}$$

At the dayside- and nightside merging gaps, the electric field induced by magnetic flux transfer across the boundary, due to reconnection, is given by $\Phi_D/l_D$ and $\Phi_N/l_N$ (S. E. Milan, 2013). The electric field is given as

$$E_\theta(\lambda_{R1}, \theta) = E_D = -V_{R1} B_r + \frac{\Phi_D}{l_D}, \pi - \theta_D < |\theta| \tag{3.11}$$

and

$$E_\theta(\lambda_{R1}, \theta) = E_N = -V_{R1} B_r - \frac{\Phi_N}{l_N}, |\theta| < \theta_N \tag{3.12}$$

Integrating around $E_\theta$ around the boundary gives the electro static potential at the region 1 currents, $\Phi_{R1}(\theta) = \Phi(\lambda_{R1}, \theta)$, as a function of the azimuth:

$$\Phi_{R1}(\theta) = -R_E \sin \lambda_{R1} \int_0^{2\pi} E_\theta(\lambda_{R1}, \theta) d\theta \tag{3.13}$$

We can calculate the electrostatic potential going along the OCB $\Phi_{R1}(\theta)$ for different azimuths. Depending on the longitudinal region the expression for the electrostatic potential changes. The functional form is listed in Table 1, below.

Table 3.1: $\Phi_{R1}$ as a function of $\theta$.

| $\theta$ | $\Phi_{R1}(\theta)$ |
|---|---|
| $0 < \theta < \theta_N$ | $-R_E \sin \lambda_{R1}\{E_N \theta\}$ |
| $\theta_N < \theta < \pi$ - $\theta_D$ | $-R_E \sin \lambda_{R1}\{(E_N - E_B)\theta_N + E_B \theta\}$ |
| $\pi$ - $\theta_D < \theta < \pi + \theta_D$ | $-R_E \sin \lambda_{R1}\{(E_N - E_B)\theta_N + (E_D - E_B)(\theta_D - \pi) + E_D \theta\}$ |
| $\pi + \theta_D < \theta < 2\pi$ - $\theta_N$ | $-R_E \sin \lambda_{R1}\{(E_N - E_B)\theta_N + 2(E_D - E_B)\theta_D + E_B \theta\}$ |
| $2\pi$ - $\theta_N < \theta < 2\pi$ | $-R_E \sin \lambda_{R1}\{2(E_N - E_B)(\theta_N - \pi) + 2(E_D - E_B)\theta_D + E_N \theta\}$ |

By way of examples we can observe two different cases. We use the same values as done by [Milan, 2013] to ensure that we are able to reproduce the same potential around

the boundary. In case a) we use the following values $\Phi_D = 50$kV, $\Phi_N = 0$kV and $F_{PC} = 0.4$GWb while for case b) we use $\Phi_D = 30$kV, $\Phi_N = 70$kV and $F_{PC} = 0.7$GWb.

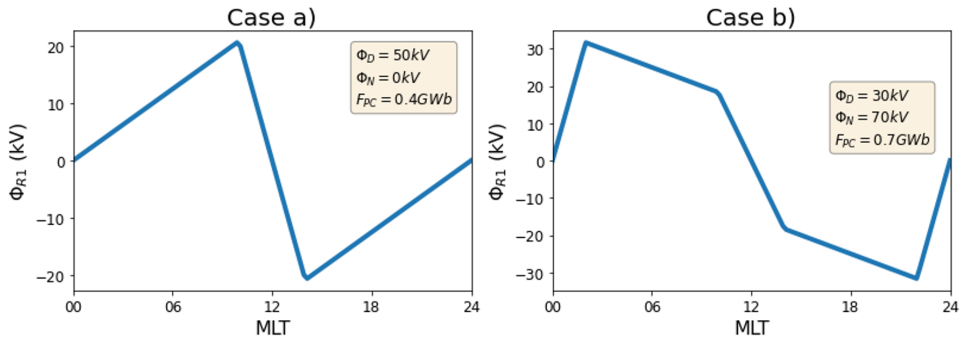


Figure 3.3: The electrostatic potential calculated for the OCB at different azimuths. Case a): $\Phi_D = 50$kV, $\Phi_N = 0$kV and $F_{PC} = 0.4$GWb. Case b): $\Phi_D = 30$kV, $\Phi_N = 70$kV and $F_{PC} = 0.7$GWb.

In these examples Milan [2013] has used these values for the throats of both day- and nightside merging gaps. $\theta_D = \theta_N = \frac{\pi}{6}(30°)$. The region 2 field aligned currents are at a set distance equatorwards from the region 2 current system $\Delta\lambda$. so that $\lambda_{R2} = \lambda_{R1} + \Delta\lambda$. In Heppner-Maynard boundary domain $\lambda > \lambda_{R2}$ there is no convection, so

$$\Phi_{R2}(\theta) = \Phi(\lambda_{R2}, \theta) = 0 \tag{3.14}$$

The boundary conditions used to solve equation (3.3) are the conditions set for $\Phi_{R1}$ and $\Phi_{R2}$. The full solution include the three regions $\lambda < \lambda_{R1}$, the polar cap region, $\lambda_{R1} < \lambda < \lambda_{R2}$, the return flow region and $\lambda > \lambda_{R2}$, the low-latitude region. Shown by *Freeman* [2003], the solution for the equation is made easier by the substitution $\Lambda = log_e tan\frac{1}{2}\lambda$ where $\frac{d\Lambda}{d\lambda} = (sin\lambda)^{-1}$. Equation (3.3) becomes

$$\nabla^2\Phi = \frac{\partial^2\Phi}{\partial\Lambda^2} + \frac{\partial^2\Phi}{\partial\theta^2} = 0 \tag{3.15}$$

The solutions for the different domains is now given as

$$\Phi_{PC}(\Lambda, \theta) = \sum_{m=1}^{N} s_m \sin\, m\theta\, e^{m(\Lambda - \Lambda_{R1})} \tag{3.16}$$

$$\Phi_{RF}(\Lambda,\theta) = \sum_{m=1}^{N} s_m \sin\, m\theta \, \frac{\sinh\, m(\Lambda - \Lambda_{R2})}{\sinh\, m(\Lambda_{R1} - \Lambda_{R2})} \tag{3.17}$$

$$\Phi_{LL}(\Lambda,\theta) = 0 \tag{3.18}$$

$s_m$ are coefficients of Fourier expansion of $\Phi_{R1}$, which we reduce to $N = 20$ for numerical reasons. This is to avoid impractically long run times for our script. $s_m$ is calculated from

$$s_m = \frac{1}{\pi}\int_0^{2\pi} \Phi_{R1}(\theta) \sin\, m\theta d\theta \tag{3.19}$$

To fully describe the electrical field components we require the spatial derivative of the electrostatic potential for the polar cap region and return flow region. That is given by the following result (S. E. Milan, 2013).

$$\frac{\partial \Phi_{PC}}{\partial \Lambda}(\Lambda,\theta) = \sum_{m=1}^{N} s_m \sin\, m\theta \, e^{m(\Lambda - \Lambda_{R1})} \tag{3.20}$$

$$\frac{\partial \Phi_{PC}}{\partial \theta}(\Lambda,\theta) = \sum_{m=1}^{N} s_m \cos\, m\theta \, e^{m(\Lambda - \Lambda_{R1})} \tag{3.21}$$

$$\frac{\partial \Phi_{RF}}{\partial \Lambda}(\Lambda,\theta) = \sum_{m=1}^{N} s_m \sin\, m\theta \, \frac{\cosh\, m(\Lambda - \Lambda_{R2})}{\sinh\, m(\Lambda_{R1} - \Lambda_{R2})} \tag{3.22}$$

$$\frac{\partial \Phi_{RF}}{\partial \Lambda}(\Lambda,\theta) = \sum_{m=1}^{N} s_m \cos\, m\theta \, \frac{\sinh\, m(\Lambda - \Lambda_{R2})}{\sinh\, m(\Lambda_{R1} - \Lambda_{R2})} \tag{3.23}$$

Then the electrical field components are given as

$$E_\lambda = -\frac{1}{R_E \sin\lambda}\frac{\partial \Phi}{\partial \Lambda} \tag{3.24}$$

$$E_\theta = -\frac{1}{R_E \sin\lambda}\frac{\partial \Phi}{\partial \theta} \tag{3.25}$$

Further expanding on the two cases, case a) and b), we still use the following values $\Phi_D = 50\text{kV}$, $\Phi_N = 0\text{kV}$ and $F_{PC} = 0.4\text{GWb}$ while for case b) we use $\Phi_D = 30\text{kV}$,

$\Phi_N = 70$kV and $F_{PC} = 0.7$GWb. We also include that the co-latitudinal distance between region 1 and region 2 is $\Delta\lambda = \frac{\pi}{18}(10°)$.

By using pcolormesh in Python we reproduce the two cases presented by (S. E. Milan, 2013), to ensure that our model is implemented correctly.

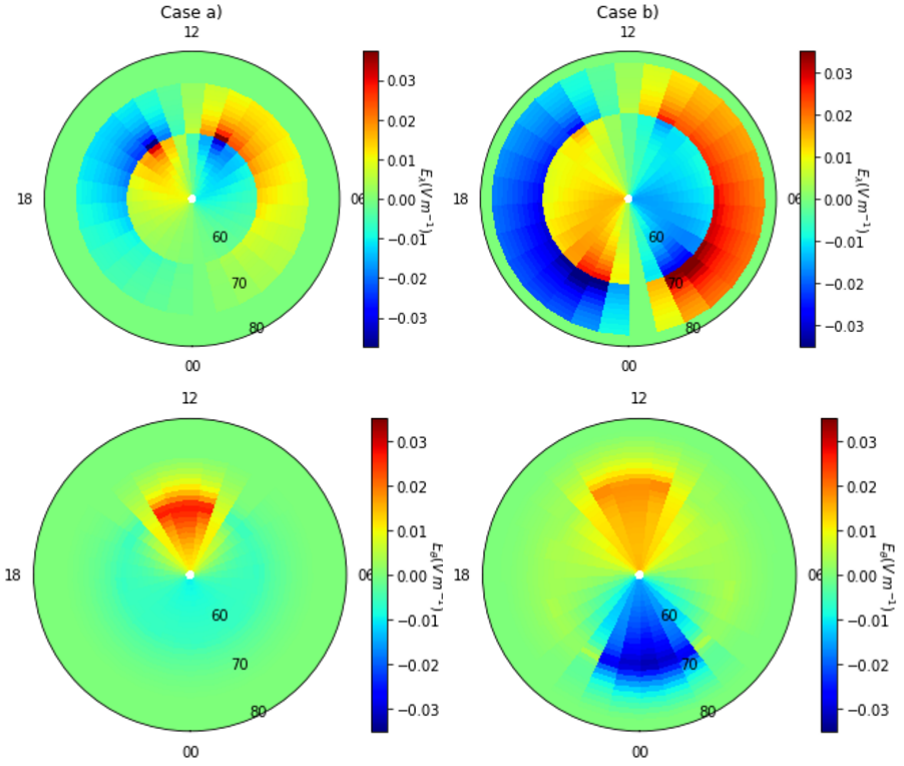


Figure 3.4: The output of our model for the two cases a) and b), the electrical field components on a MLT grid. Case a): $\Phi_D = 50$kV, $\Phi_N = 0$kV and $F_{PC} = 0.4$GWb. Case b): $\Phi_D = 30$kV, $\Phi_N = 70$kV and $F_{PC} = 0.7$GWb. For both cases $\theta_D = \theta_N = 30°$, $\Delta\lambda = 10°$..

For direct comparison we have included the plots produced by Milan (2013) in Figure 3.5.

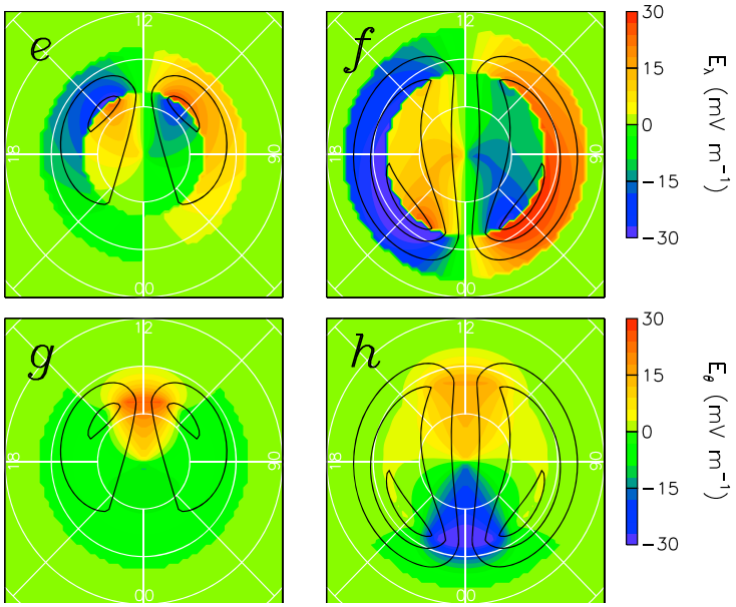


Figure 3.5: The electric field components as presented by Milan (2013). The same values for the the polar cap flux and reconnection rates are used.

The plasma convections motion is given by $\boldsymbol{V} = \frac{\boldsymbol{E}\times\boldsymbol{B}}{B^2}$, the horizontal components of the ionospheric flow vector now becomes

$$V_\lambda = -\frac{E_\theta}{B_r} \tag{3.26}$$

$$V_\theta = \frac{E_\lambda}{B_r} \tag{3.27}$$

### 3.1.2 Tracing the plasma convection

To track the evolution of polar cap patches we introduce tracer particles to our model. The purpose of tracer particles is to follow the flow of a polar cap patch. At the start of our model we assume an initial open flux $F_{PC}$ in the polar cap and calculate the position of the OCB for the polar cap flux value, given as an argument. We assume the same initial polar cap flux as presented by Milan (2013) 0.4GWb. We place tracers, starting from the calculated boundary, and place seven particles that are evenly distributed for MLT hour intervals. Studies done by Milan (2013) and Follestad et al. (2019) show we expect a twin-cell convection pattern (S. E. Milan,

2013; Follestad et al., 2019). To verify that our tracer particles behave like the models ours is based on we observe their motion for a time series of day- and nightside reconnection rates that are based on values used by Milan (2013). The time-series last for four hours and we will be using a time step of 2 min. Reconnection rates are some what arbitrary, but they are such that the magnetosphere open fluzx is set to 0.4GWb and increasing to about 0.7GWb as dayside reconnection dominates before closing out at 0.3GWb (S. Milan, Provan & Hubert, 2007). The dayside reconnection rate is assumed to linearly increase and decrease proportionally with the same rate, similarly for the nightside reconnection.

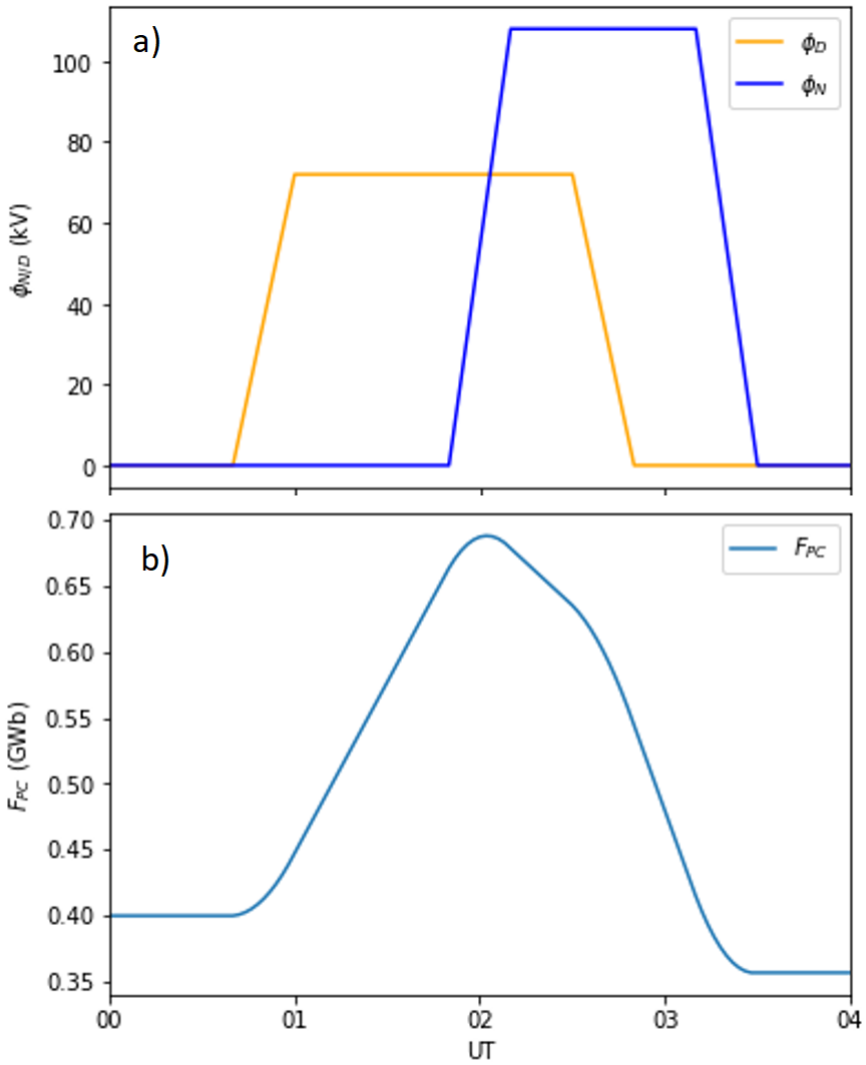


Figure 3.6: a) shows a time series for both day- and nightside reconnection rates. They increase linearly and decrease with the same rate as they increased. Our values are somewhat arbitrary, but values are made to resemble the case studied by Milan (2013), this is to easier verify the legitimacy of our own model. b) the polar cap flux values for a time series of the same timespan as in a). The rate of change in the polar cap flux is calculated by use of equation (3.7) where $dt = 120$s.

We have used equation (3.7) to calculate the rate of change in polar cap flux $F_{pc}$.

To further study how our version of the ECPC model holds up we observe how a tracer particle behaves when placed at the dayside OCB when introducing the reconnection rate time series.

### 3.1.3 Proof of concept

Earlier we mentioned how a twin-cell convection pattern is predicted the Dungey cycle. We would due to E×B-drift in the polar cap (Siscoe & Huang, 1985) expect the same pattern from our tracer particles. Their velocities are given by equations 3.26 and 3.27, and use these to update the current positions through equations 3.28 and 3.29 shown below

$$\lambda_{n+1} = \lambda_n + V_{\lambda,n+1} * \frac{\Delta t}{R_E} \tag{3.28}$$

$$\theta_{n+1} = \theta_n + V_{\theta,n+1} * \frac{\Delta t}{R_E * \sin \lambda_n} \tag{3.29}$$

Where $n$ is the current time step, $\Delta t = 120$s and $\mathrm{R}_E$ is the Earth radii.

We are also interested in their mean velocities, this can be calculated through equation 3.30 and taking the mean of all velocities for the tracer of interest.

$$V = \sqrt{V_\theta^2 + V_\lambda^2} \tag{3.30}$$

We ultimately want to store the values for the tracer particles as they travel from the dayside merging gap to the nightside merging gap. To do this a condition must be set. The tracer particle has reached the nightside merging gap when its co-latitudinal positions are the same, or larger, than the current calculated OCB for the polar cap flux. The tracer position also has to be at longitudinal values that are to that of the nightside meaning $\theta <$ 18MLT or $\theta >$ 06MLT. When we have confirmed that this condition works as intended we continue by studying 1000 tracers starting at the OCB, evenly spaced between the locations 09MLT to 15MLT. These are locations where plasma reservoirs are usually located.

We will track the propagation time of every tracer and study what the propagation time distribution looks like for different reconnection rate time series. We therefore introduce synthetically generated time series, generated by Nguyen et al. (2021). How these reconnection rates were generated are thoroughly explained in (Nguyen, 2021). We are given 10 sets of reconnection rates per IMF interval, there are 10 IMF intervals and one time series lasts 90 minutes. We will be using the mean value of the

10 sets to represent one IMF interval and we will also be concatenating these time series to generate time series lasting 3 hours, better matching the observed patch propagation time of 2-3 hours, observed by Oksavik et al. (2010).

# Chapter 4

# Results

In the coming chapter we will present the results produced by our ECPC model, explained in section 3.1, when we introduce the synthetic reconnection rates generated by Nguyen (2021). These results include the electric field components for the $\theta$- and $\lambda$-direction, the path of our tracer particles, their mean velocities and estimated propagation time. Longitude- and co-latitude are represented by $\theta$- and $\lambda$ respectively.

As a proof of concept for our model, we reproduce the electric field components presented by Milan (2013), and confirm that our tracer particles behave as expected. They follow a twin-cell convection pattern, as explained in subsection 3.1.3. After this is verified we introduce the generated reconnection values and keep our initial open flux at 0.4GWb, also used by Milan (2013) and Follestad et al. (2019) in their studies.

The reconnection rates in use are synthetically generated time series for 10 different intervals of incoming IMF and for each interval there are dayside and nightside reconnection rates that last for 90 minutes, with a time step of 2 minutes. There are 10 time series for 1 IMF, we take the mean of the time series to calculate a reconnection rate that we use to represent the one IMF. The IMF interval is categorised within three strength classes strong, moderate and weak (Nguyen, 2021). By concatenating these values we are able to reproduce different cases of incoming IMF and increase their duration by 90 minutes.

We have performed seven different case studies where we study how a polar cap patch propagates across the northern hemisphere. Our results are a product of applying different reconnection rate time series into the ECPC paradigm. The very first will include a study of the time series of reconnection rates similar to those studied by Milan (2013). These reconnection rates, that were used as a proof of concept for our model, presented in Figure 3.6 and will be re-introduced later during this case study.

The three next cases will simulate a incoming IMF with a southward directed magnetic field line turning northward with a similar strength classification. The following, fifth case, is a scenario where we observe a northward strong IMF, turning to a strong southward IMF, turning to a weak southward IMF before finally turning to a weak southward IMF. The two final cases are similar to the second and fourth case study, but we add an an offset of 50kV to the reconnection rates for cases B and D. Viscous interaction between the solar wind and the Earth's magnetosphere are on top of reconnection and is another phenomena driving convections. It is always present and therefore we can add a continuous offset to the reconnection rates (Axford, 1964). 50kV is the maximum predicted potential due to this phenomena (Bruntz, Lopez, Wiltberger & Lyon, 2012) and is the value we will be adding. We will discuss our reasoning, for introducing an offset, further in chapter 5. Common for all cases are that the seven tracer particles will start at the OCB with particle #0 starting at 10MLT and particle #6 starting at 15MLT with the others evenly spaced in-between. Also common for all cases is that we will be studying three events that we all label event *a*, *b* and *c*, they are snapshots in in time. The time of the event will be based on the higher reconnection rate values as the showcase the strengths the electrical field components could exert.

## 4.1 Case A: assuming reconnection time series similar to previous case study

For this case we re-introduce the time series presented by Milan (2013). The reconnection rates in use are presented in Figure 4.1, along with the calculated polar cap flux below in the same figure. The three events are picked to be prior to the increase of polar cap flux, at the peak and towards the bottom after a decrease in the polar cap flux. The time for these events are 3600s (01:00 UT), 7200s (02:00 UT) and 12480s (03:28 UT) respectively.

Figure 4.2 showcase six snapshots of the electric field. Six are needed to visualise the three events, since the electric field is expressed through two components. These electric fields are calculated by equation 3.24 and 3.25. We are able to observe in the $\lambda$-component that the direction of the field outside the OCB is opposite of that inside the OCB, leading to sunwards plasma drift which characteristic of the return flow region (S. Milan, Lester, Greenwald & Sofko, 1999). There is clear expansion for the electric field between events *a* and *b*., while between events *b* and *c* there is a clear contraction. During event *a* there is only dayside reconnection, seen in Figure 4.1, and this can clearly be seen in the corresponding electrical fields as there is mainly activity on the dayside. During event *b* the nightside reconnection rate is now present as the two reconnection rates approach each other the expansion of the electrical fields starts to stop and starts contracting as the nightside reconnection rate starts to dominate. During the snapshot of this event we see more activity towards

both the day- and nightside as neither reconnection rates are 0 anymore. During the final event, event *c*, there is no more dayside reconnection and barely any nightside reconnection as the latter starts approaching 0kV. The lack of activity is seen in the electrical fields in Figure 4.2 .

In Figure 4.3 we can see similar behaviour in the tracer particles for the first two snapshots, but in event *c* the tracer particles has finally crossed the nightside OCB and has started to curve towards the dayside as observed in the velocity vector fields for all previous cases. Though, particle #6, and others that are closer to 06MLT and 18MLT, behave rather odd. particle #0 and #5 both propagate towards the nightside boundary, but follow the expansion and contraction of the OCB, causing them to travel outwards and inwards. Particle #6 on the other hand, starting at MLT15, does not follow any clear twin-cell convection pattern. This is also due to the expansion and contraction of the OCB, as the OCB starts to contract the particle is not able to keep up and gets transported into the return flow region and start propagating back towards the dayside OCB. This leads to the particle returning in a curved path and on the inside of the path of particle #5. The first tracers to arrive at arrive after 7800s (02:10 UT) and the latter tracers to arrive, out of the seven, arrive after 8160s (02:16 UT).

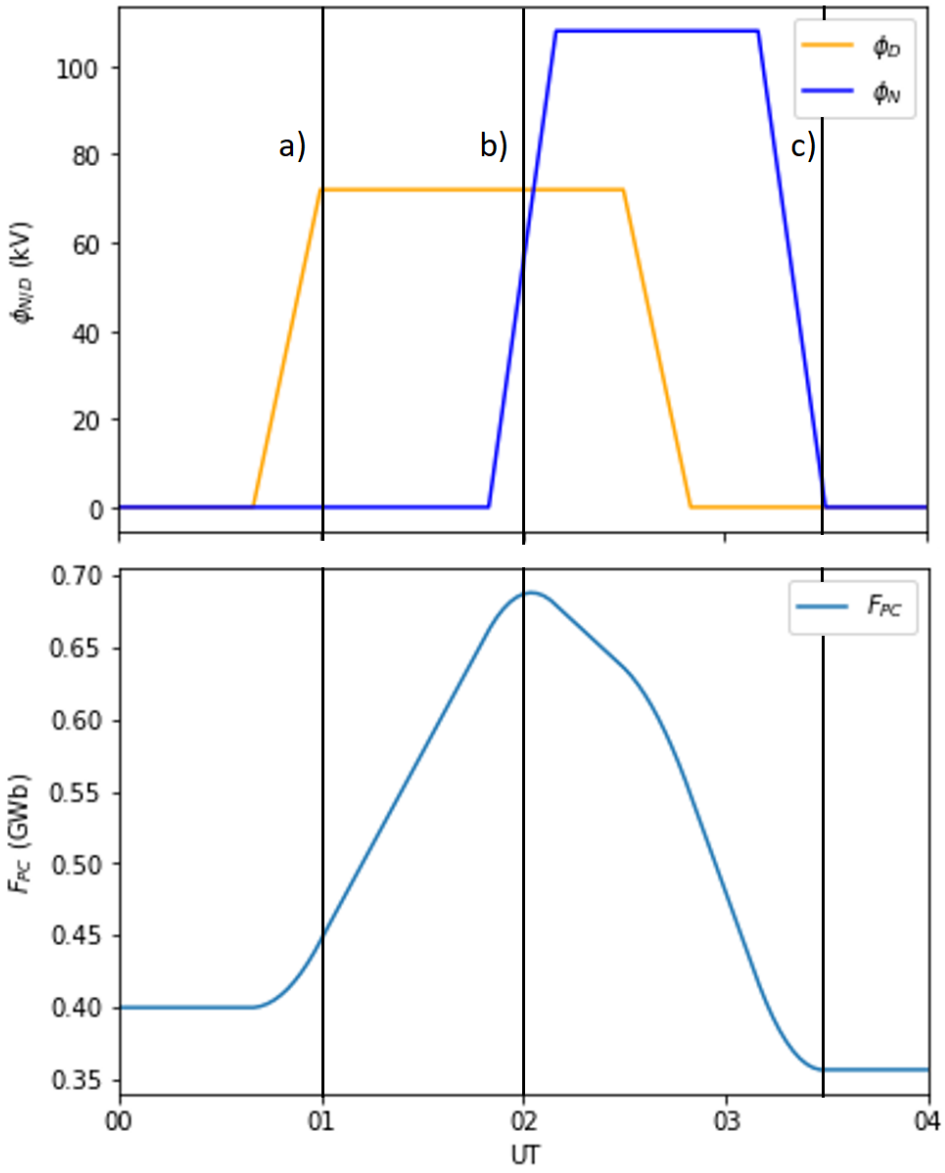


Figure 4.1: During event $a$ dayside reconnection dominates with a value of 70kV before nightside reconnection becomes more prominent in $b$, steadily increasing to 115kV. $c$ takes place after nightside reconnection has dominated. Polar cap flux ($F_{pc}$) with initial value 0.4GWb increasing during event $a$ before reaching a local maximum right after event $b$ and declining below the initial value in event $c$.

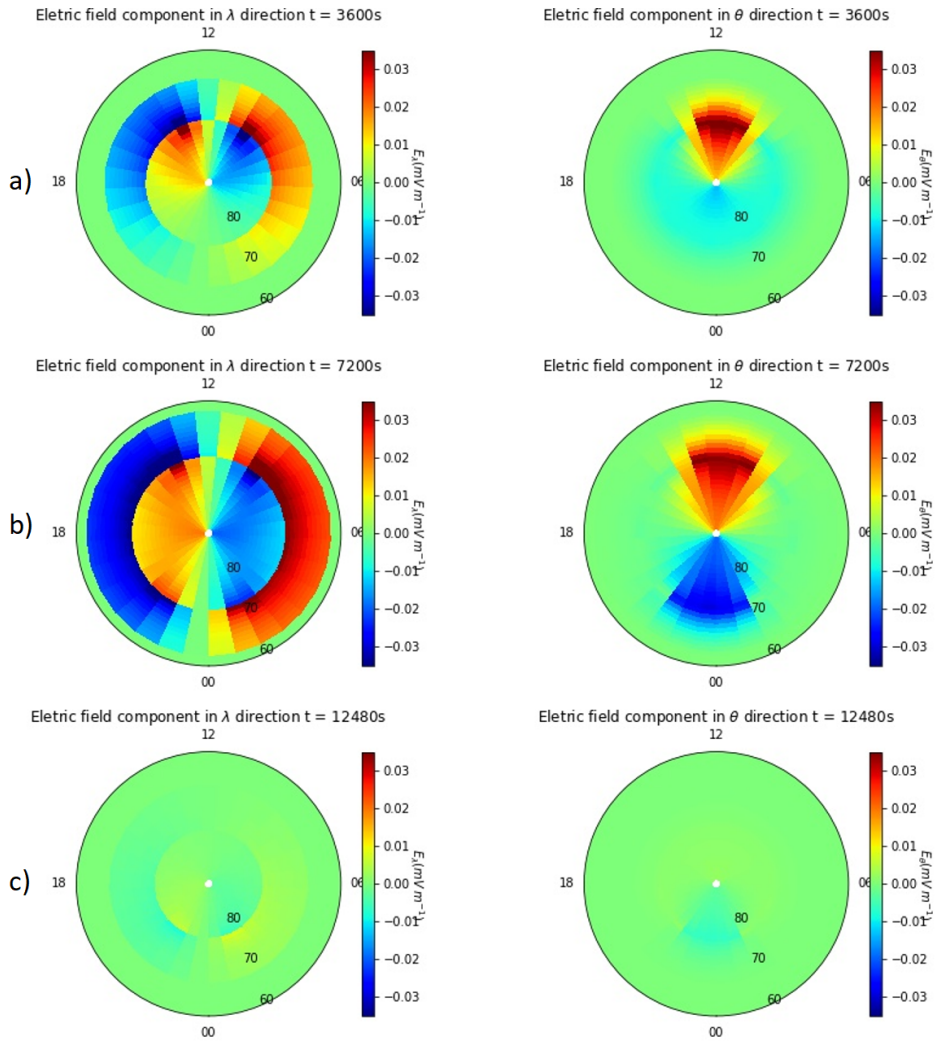


Figure 4.2: The calculated electric field components for $\lambda$ and $\theta$. In event $a$ to $b$ we observe a significant expansion before a significant contraction in event $b$ to $c$. Values range between 35mV/m and -35mV/m.

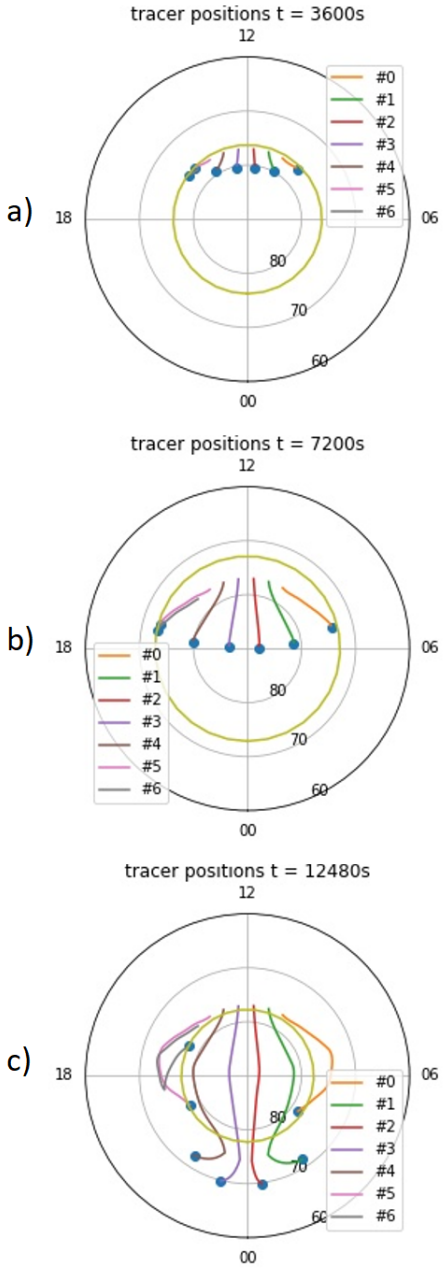


Figure 4.3: Tracer paths allowing us to see the current position of each tracer for each snapshot and also the path they have travelled. We observe signs of twin-cell convection pattern and within the given time some reach the nightside OCB. The OCB is marked by the yellow line.

In Table 4.1 the mean velocities of each tracer particle. We need to keep in mind, for the first time steps of this case there are no reconnection rates, leading to the tracer particles having velocities 0m/s for some time and the same applies towards the end of the time series.

Table 4.1: Calculated mean velocity for each tracer particle placed along the OCB. There are some time steps where both reconnection rates are set to 0kV, these steps have been excluded in the calculation of the mean velocities. Starting position for tracer #0 is at 10MLT while tracer #6 starts at 15MLT.

| Tracer # | Mean velocity [m/s] |
|---|---|
| 0 | 273.4 |
| 1 | 386.2 |
| 2 | 404.7 |
| 3 | 401.3 |
| 4 | 379.6 |
| 5 | 258.4 |
| 6 | 278.0 |

## 4.2 Case B: IMF Z interval -0.5nT turning to 0.5nT

Figure 4.4 shows the mean of the generated reconnection rates for an incoming IMF for values [-0.73, -0.02)nT turning northward after 90 minutes. After another 90 minutes the generated values are representative of an IMF with values [-0.02, 0.69)nT (Nguyen, 2021). These IMF values are classified as *weak* IMF. Also in Figure 4.4, below, is the calculated polar cap flux, using equation 3.7. Within the first 90 minutes we can observe that the polar cap flux goes from decreasing to increasing as the nightside reconnection dominates the first half, before the dayside reconnection rate starts dominating in the latter. After 90 minutes we see a similar pattern as nightside reconnection dominates again before dayside reconnection rates starts dominating, increasing the polar cap flux. The polar cap will be contracting before expanding as dayside reconnection starts to dominate, before contracting a second time when nightside reconnection dominates again (Rostoker et al., 1980). We further study three events through our snapshots that now are the times 3360s (00:56 UT), 6120s (01:42 UT) and 10320s (02:52 UT)

Figure 4.5 are six snapshot of the events *a,b* and *c* showcasing the electric field components. We are able to observe in the $\lambda$-component that the return flow region is still present for latitudes lower that than the OCB. We are able to see that in event *a* there is mostly activity on the nightside and this lines up well with the values for *a* in Figure 4.4, while in event *b* there is slight less activity on the nightside and far more on the dayside, which also lines up with event *b* 4.4. We are also able to see that between event *a* and *b* the electric fields are expanding.. Then it starts contracting

between event *b* and *c*. Values observed range from 20mV/m and -20mV/m.

Figure 5.2 are three snapshots of the same events, *a,b* and *c*, and the current location of the seven tracer particles, along with their path. Their starting locations are along the OCB with tracer #0 located at 10MLT and the last, #6, located at 15MLT with every tracer evenly spaced in-between. We are able to see, from event *a*, that they are propagating from the dayside, towards the nightside, in the direction of the geomagnetic north pole. In events *b* and *c* we observe similar behaviour to event *a*, but they propagate closer to the nightside OCB for each event. We also see that by event *c* they are nowhere close to the nightside OCB.

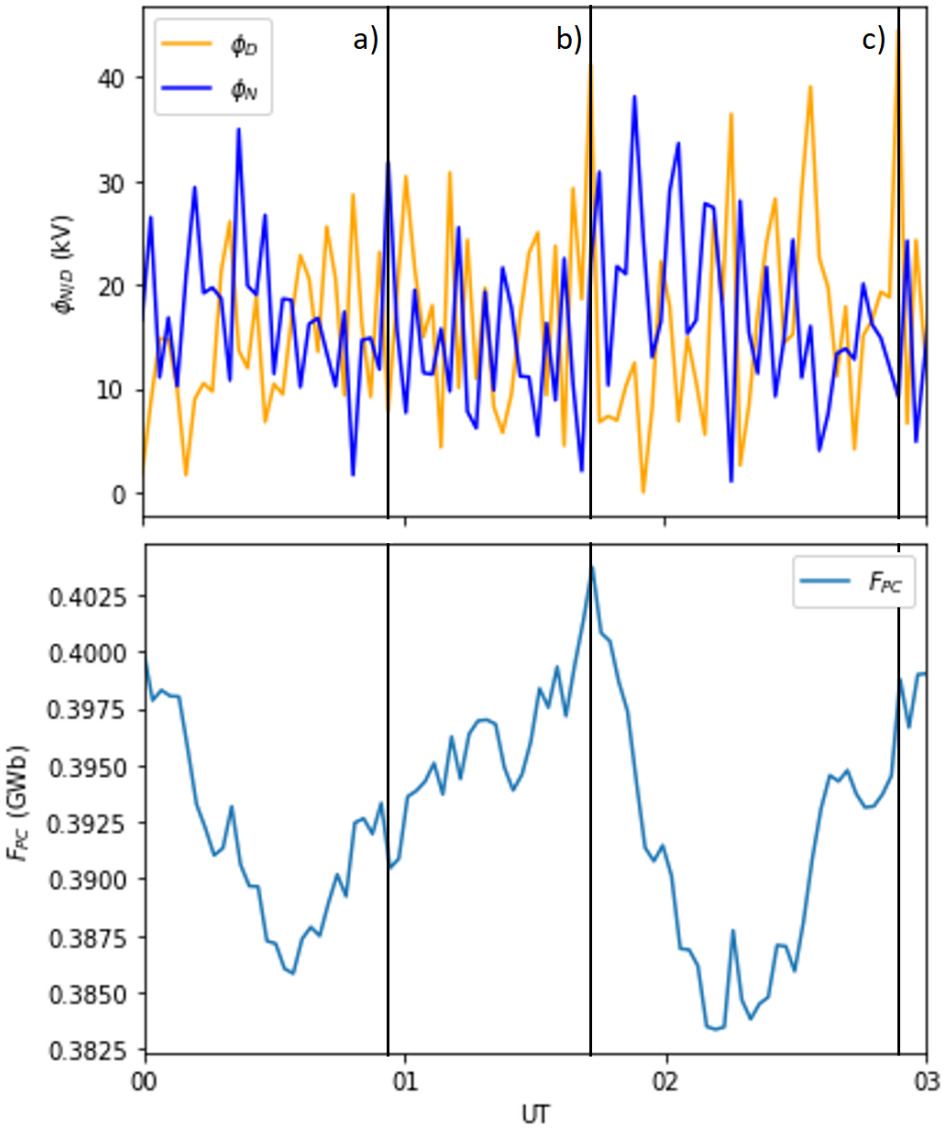


Figure 4.4: Generated reconnection rates ($\Phi_{D/N}$), the first 90 minutes are equivalent of an IMF with values in the interval the [-0.73, -0.02)nT and for the second 90 minutes for the interval [-0.02, 0.69)nT. Polar cap flux ($F_{pc}$) with initial value 0.4GWb. Events $a$,$b$ and $c$ are snapshots represented by black vertical lines.

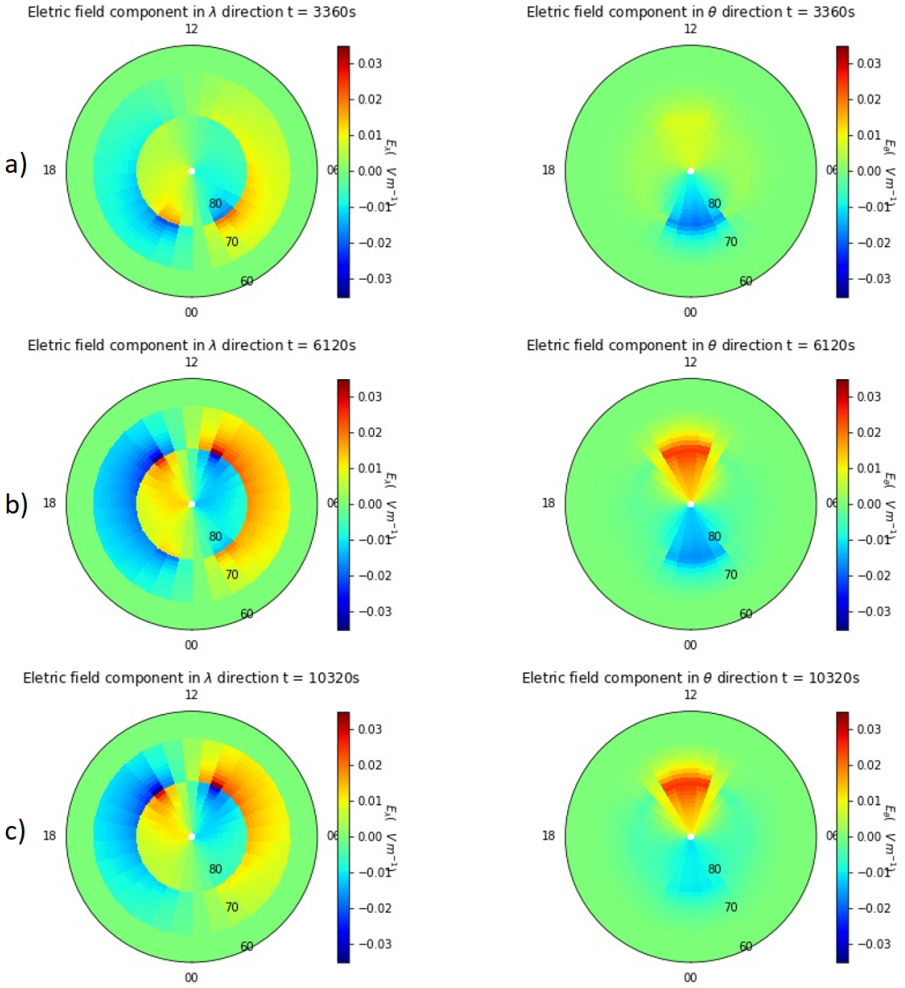


Figure 4.5: The calculated electric field components for $\lambda$ and $\theta$. In event $a$ to $b$ we observe a slight expansion before a slight contraction in event $b$ to $c$.

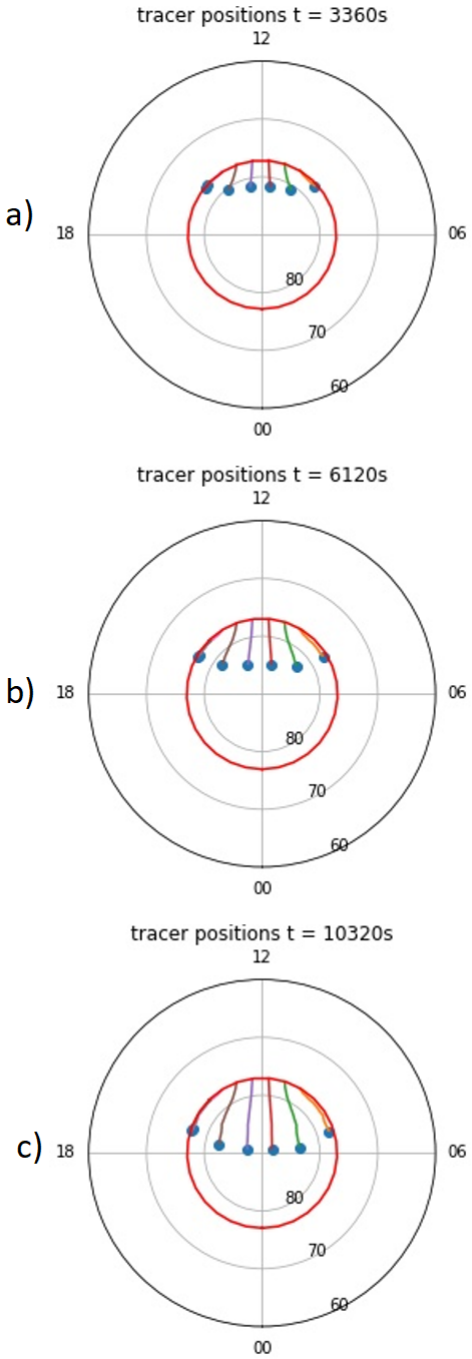


Figure 4.6: Tracer paths allowing us to see the current position of each tracer for each snapshot and also the path they have travelled. The OCB is marked by the red line.

In figure 5.2, event *c*, we observe that the tracer particles have yet to cross the geomagnetic north pole. We therefore calculate the individual mean velocity of each tracer particle and present them in Table 4.2. These values are calculated by calculating the velocity, given by equation 3.30, and then calculating the mean.

Table 4.2: Calculated mean velocity for each tracer particle placed along the OCB for weak IMF in the intervals [-0.73, -0.02)nT and [-0.02, 0.69)nT. Starting position for tracer #0 is at 10MLT while tracer #6 starts at 15MLT.

| Tracer # | Mean velocity [m/s] |
|---|---|
| 0 | 99.0 |
| 1 | 124.1 |
| 2 | 131.4 |
| 3 | 130.5 |
| 4 | 120.7 |
| 5 | 93.4 |
| 6 | 88.2 |

## 4.3 Case C: IMF Z interval -2.0nT turning to 2.0nT

Figure 4.7 shows the mean of the generated reconnection rates for an incoming IMF for values [-2.48, -1.51)nT turning northward after 90 minutes. We assume that the IMF has made a leap to a much larger value by concatenating these values. After 90 minutes the generated values are representative of an IMF with values [1.47, 2.50)nT (Nguyen, 2021).They are both in the strength category *moderate*. Below in Figure 4.7 is the calculated polar cap flux, using the same equation as in Case B. Within the first 90 minutes we can observe the polar cap flux steadily increasing as the dayside reconnection dominates for a majority of the time. After another 90 minutes there is a slight decline before increasing slightly. The reconnection rate values do not seem to differ too much from Case B, despite being categorised as stronger IMF. We want to further study three and observe the timer0s (00:00 UT), 6340s (01:46 UT) and 9000s (02:30 UT) respectively. Event *a* is to study the initial state of the electrical field.

Figure 4.8 are the six snapshots of the events *a,b* and *c*. The initial values are rather low, as the reconnection rates has low values for this event in Figure 4.7. Events *b* and *c* has some of the largest values for the reconnection rates and the electric field has values of 25mV/m to -25mV/m, which are larger than that of Case B.

Figure 5.2 are thee snapshots of the same events and the current location of the seven tracer particles, along with their path. We are able confirm, from event *a*, that the tracer do start at the dayside OCB for the generated reconnection rates too. Event *b* also confirm that they still propagate towards the nightside OCB, but by event *c*

they are still not close to reaching the nightside OCB.

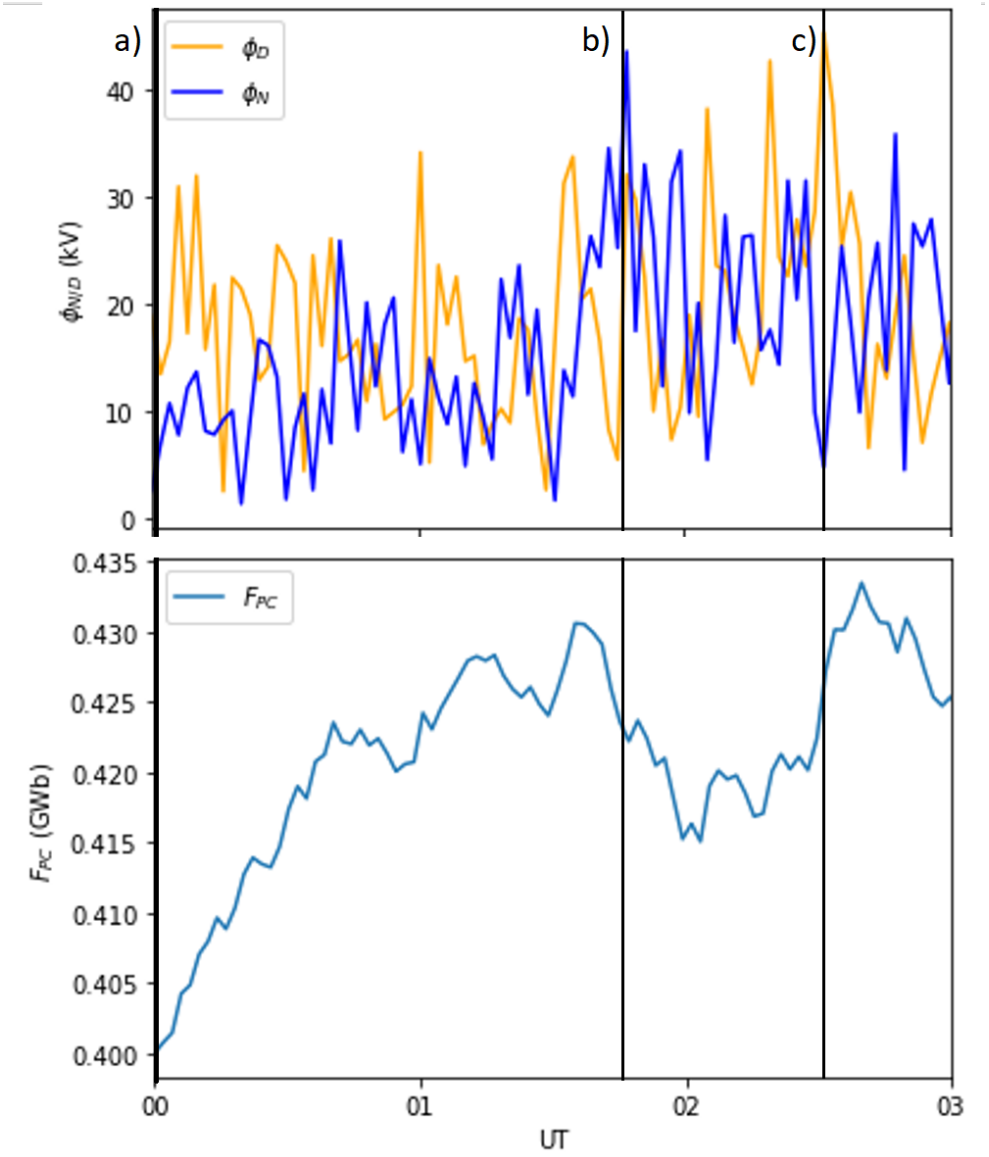


Figure 4.7: Generated reconnection rates ($\Phi_{D/N}$), the first 90 minutes are equivalent of an IMF with values in the interval the [-2.48, -1.51) and for the second 90 minutes for the interval [1.47, 2.50)nT. Polar cap flux ($F_{pc}$) with initial value 0.4GWb below. Events *a*,*b* and *c* are snapshots represented by black vertical lines with event *a* being visualized with a bold line at 00:00 UT.

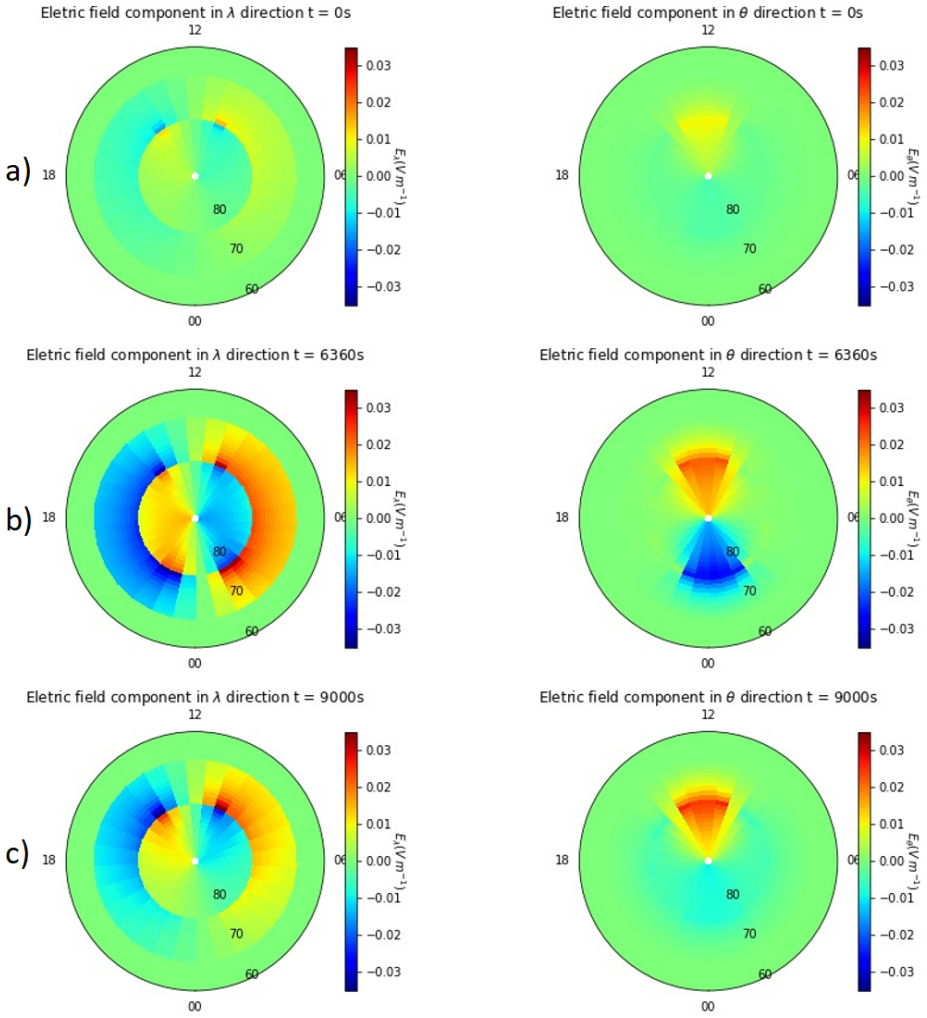


Figure 4.8: The calculated electric field components for $\lambda$ and $\theta$. For all three events there is a slight expansion.

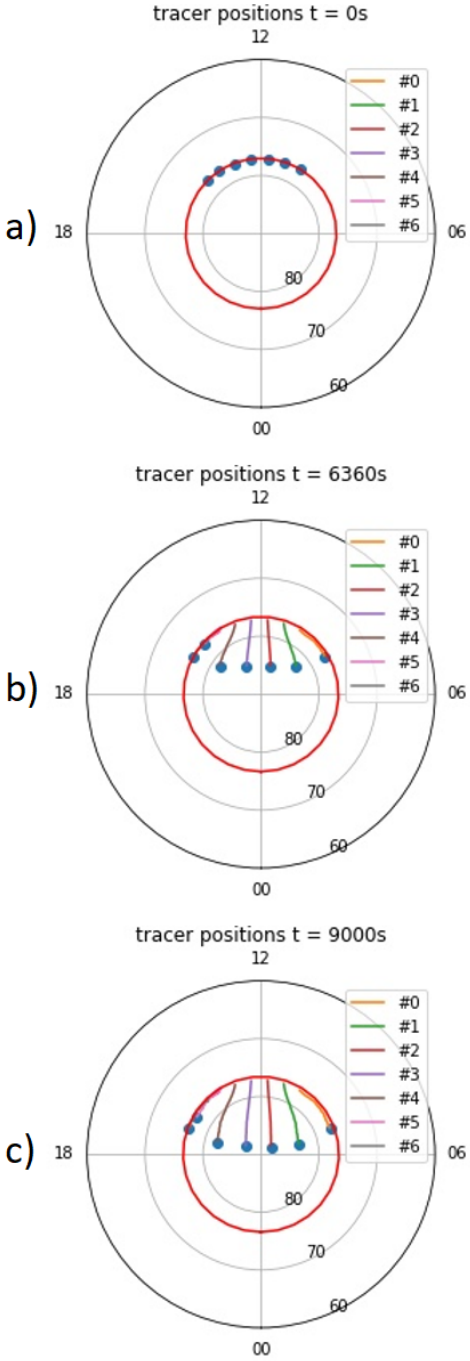


Figure 4.9: Tracer paths allowing us to see the current position of each tracer for each snapshot and also the path they have travelled. The OCB is marked by the red line. The slight expansion of the polar cap flux is easier to be seen by comparing the longitudinal position of the red line between each event.

In figure 5.2, event *c*, we again observe that the tracer particles have yet to cross the geomagnetic north pole and we check the mean velocity of each tracer particle and tabulate them into Table 4.3. We here observe that the mean velocity does not differ too much from the values in Table 4.2, but are barely higher than that of Case B.

Table 4.3: Calculated mean velocity for each tracer particle placed along the OCB for moderate IMF in the intervals [-2.48, -1.51)nT and [1.47, 2.50)nT. Starting position for tracer #0 is at 10MLT while tracer #6 starts at 15MLT.

| Tracer # | Mean velocity [m/s] |
|---|---|
| 0 | 105.3 |
| 1 | 131.3 |
| 2 | 139.7 |
| 3 | 138.8 |
| 4 | 127.7 |
| 5 | 133.5 |
| 6 | 92.5 |

## 4.4 Case D: IMF Z interval -5.0nT turning to 5.0nT

Figure 4.10 shows the mean of the generated reconnection rates for an incoming IMF for values [-39.00, -4.03)nT turning northward after 90 minutes and the reconnection rate represent values for an IMF in the interval [4.03, 37.70)nT (Nguyen, 2021). We now want to observe a polar cap patch propagation during what would be categorised as a *strong* IMF. Below, in Figure 4.12, is the calculated polar cap flux.. Within the first 90 minutes we observe that the polar cap flux steadily increasing as the dayside reconnection dominates, before decreasing as nightside reconnection starts to dominate. The same reverse applies after 90 minutes, as nightside reconnection continue to dominate, leading to a steady decrease in the polar cap flux before we observe dayside reconnection starting to dominate during the final minutes of the later half. The three events we now study are the times 3120s (00:52 UT), 5400s (01:30 UT) and 10080s (02:48 UT).

Figure 4.11 are shows the electric field components for the three events. Event *a* is when $\Phi_N = 70$kV, in Figure 4.10, which is the largest reconnection rate out of Case B, C and D. This leads to the electric field components having values as high as 35mV/m and -35mV/m. Other than that event there are no other time with as high of an output as this. Event *b* and *c* are during times when the reconnection rates in Figure 4.10are comparatively high to Case B and C and Figure 4.11 has values that are similar to that of the highest value outputs in the the aforementioned cases.

In Figure 4.12 the tracer particle behave similar to before, except #0, #5 and #6. We see that prior to event *a* that they have propagated through the return flow region

just like #6 in Case A. We see in Figure 4.10 that prior to this event there is a sharp decline in the polar cap flux and the contraction may have been to sudden for the particle to keep up. for events *b* and *c* we still observe similar behaviour to that of Case B and C, still not reaching the nightside OCB by the last event.

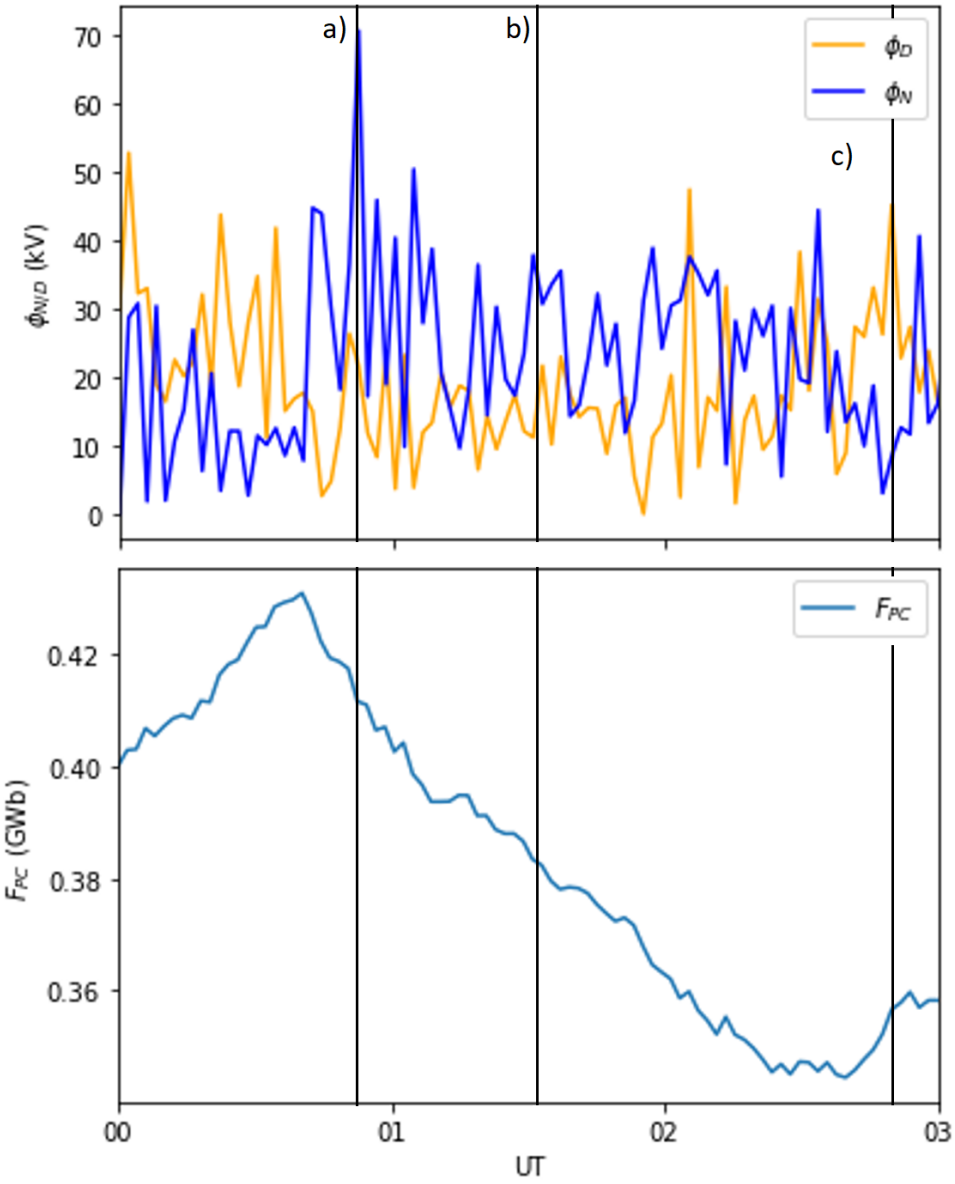


Figure 4.10: Generated reconnection rates ($\Phi_{D/N}$), the first 90 minutes are equivalent of an IMF with values in the interval the [-39.00, -4.03) and for the second 90 minutes for the interval [4.03, 37.70)nT. Values vary from close to 0kV all the way up to 70kV. Polar cap flux ($F_{pc}$) with initial value 0.4GWb can be seen bellow and it gradually decreases throughout each event.

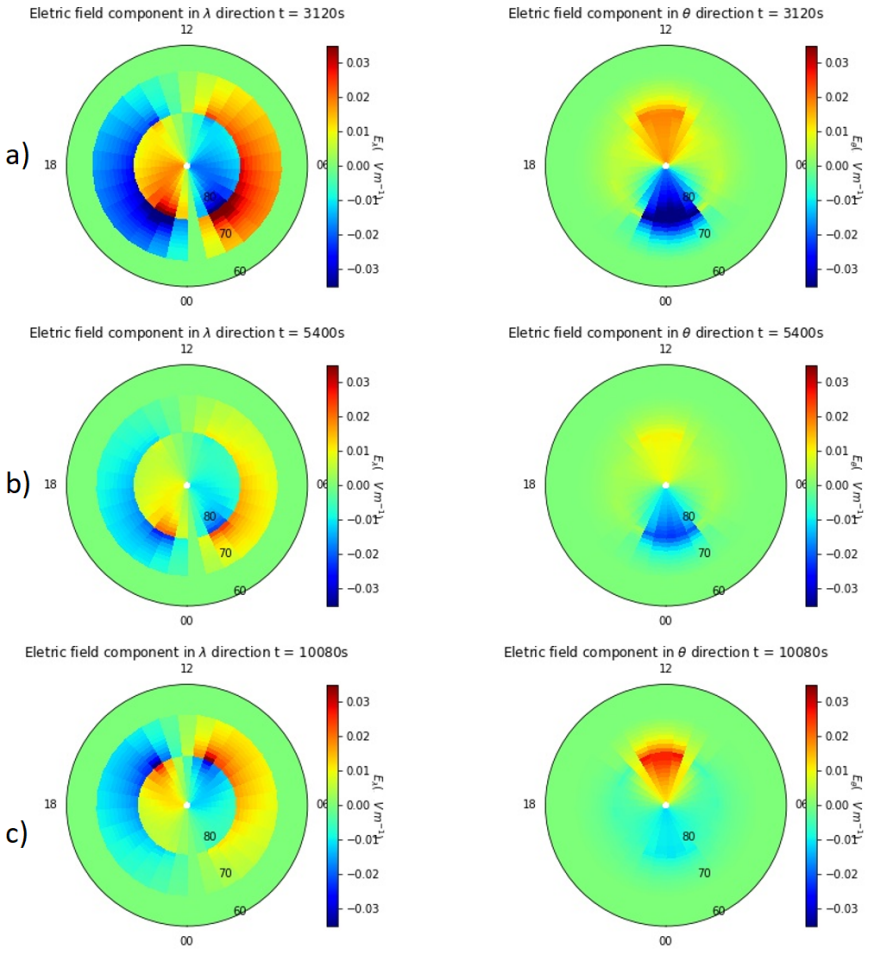


Figure 4.11: The calculated electric field components for $\lambda$ and $\theta$. There is a slight contraction in all three events.

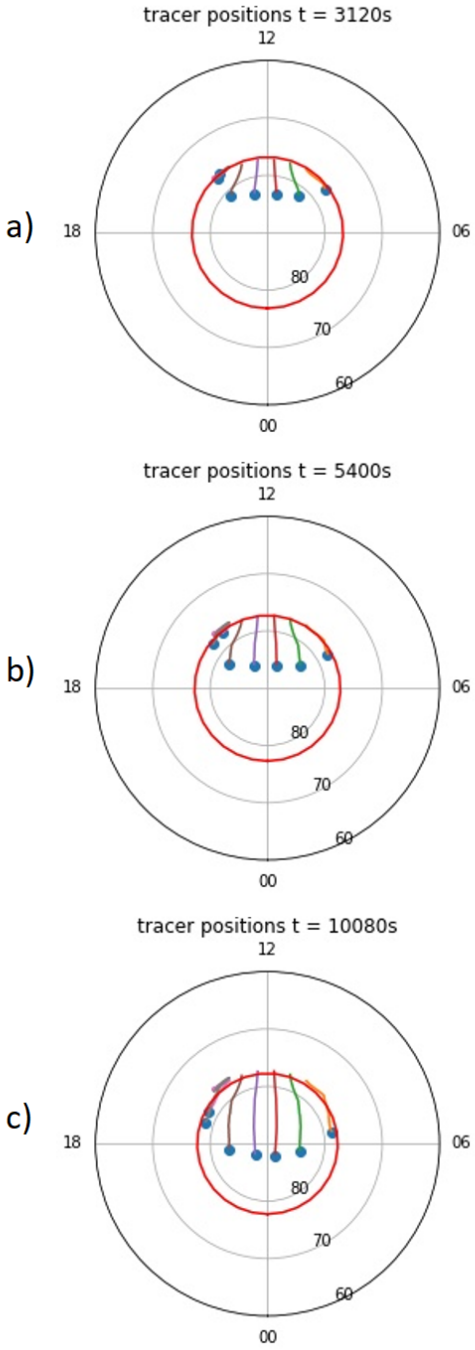


Figure 4.12: Tracer paths allowing us to see the current position of each tracer for each snapshot and also the path they have travelled. Despite the IMF being categorised as *strong* the tracer particle spend 8640s, 02:24UT, to reach halfway to the OCB. The OCB is still marked by the red line.

By the third snapshot, event $c$, in 4.12 we again observe that the tracer particles are not yet close to the nightside OCB. In comparison with the previous cases, we do notice a further distance covered, and this is confirmed by Table 4.4 as these mean velocities have significantly larger values than the previous cases.

Table 4.4: Calculated mean velocity for each tracer particle placed along the OCB for strong IMF in the intervals [-39.00, -4.03) and [4.03, 37.70)nT. Starting position for tracer #0 is at 10MLT while tracer #6 starts at 15MLT.

| Tracer # | Mean velocity [m/s] |
|---|---|
| 0 | 119.8 |
| 1 | 152.0 |
| 2 | 162.4 |
| 3 | 161.3 |
| 4 | 147.5 |
| 5 | 155.4 |
| 6 | 143.5 |

## 4.5 Case E: IMF Z interval turning from strong to weak

The three previous cases, were all studies completed by using synthetically generated reconnection rates and all three cases resulted in no tracer particles reaching the nightside OCB. For this case we concatenate four of these time series to see if a tracer passes the nightside OCB, resulting in a 6 hour time series where a strong IMF turns to a weak IMF after 3 hours. We do this by concatenating the reconnection rates for corresponding IMF intervals in this order [4.03, 37.70)nT , [-39.00, -4.03)nT , [-0.02, 0.69)nT and [-0.73, -0.02)nT. Leading to a strong northward facing IMF turning southward, before turning northwards and weak and finally turning southwards while still weak. The resulting time series is represented in Figure 4.13 with the calculated polar cap flux.

The three events we will be having a closer look at are, in order, when the tracers have propagated for half of the time series 10800s (03:00 UT), when the first tracer reaches the nightside OCB 17520s (04:52 UT) and the very end of the time series to observe how far they propagate 21600s (06:00). These events are represented in Figure 4.13 where we are also able to compare the reconnection rates and polar cap flux of a strong and weak IMF. The first half, prior to event $a$ has larger values for the reconnection rates and the polar cap flux has larger expansion and contraction. While the reconnection rates and change in polar cap flux both have smaller differences in their maximum and minimum values during the latter half, during event $b$ and $c$. Figure 4.14 shows the electrical fields during our given events. For event $a$ we are

able to observe the electrical field during the change in IMF strength, while event *b* shows what the electrical field looks like when the first tracer has crossed the nightside OCB. Event *c* is at the end of the time series. None of these events has any particularly large values that differs from Case B and D which use the same time series.

In Figure 4.15 we can observe a similar behaviour for the tracer particles that started closer to 15MLT and 10MLT to that of the same tracer particles in Case D, where the are not able to keep up with the expansion and contraction of the OCB. The reconnection rates are similar in both cases, generated for a *strong* IMF, but now we have concatenated them in opposite order as seen in we compare Figure 4.13 and Figure 4.17. During event *a* we see how far the tracers propagate during a strong IMF and they do cover more than half the distance. During event *b* we are finally able to observe that tracer #2, the first to reach the return flow region on the nightside, does so after after 4 hours and 52 minutes. This is almost two hours slower compared to normal times between 2 and 3 hours (Oksavik et al., 2010). By event *c* multiple tracers have arrived at the nightside OCB, while close, the particles that had a detour through the dayside return flow region has yet to reach the nightside OCB.

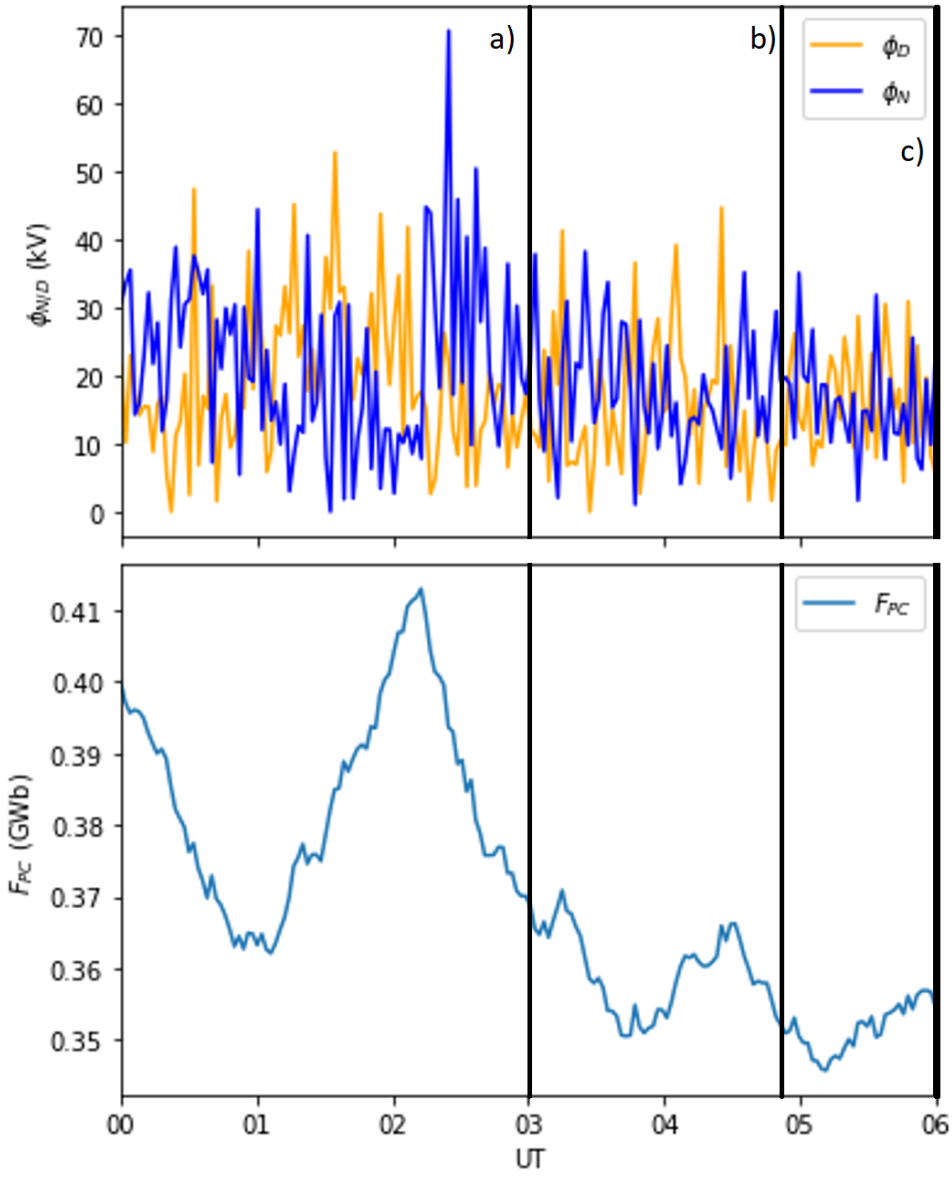


Figure 4.13: Generated reconnection rates ($\Phi_{D/N}$), the first 180 minutes emulate a strong IMF while the last 180 minutes emulates a weaker IMF. Polar cap flux ($F_{pc}$) with initial value 0.4GWb varies more the first 180 minutes during the strong IMF, compared to the latter half where the IMF is weak.

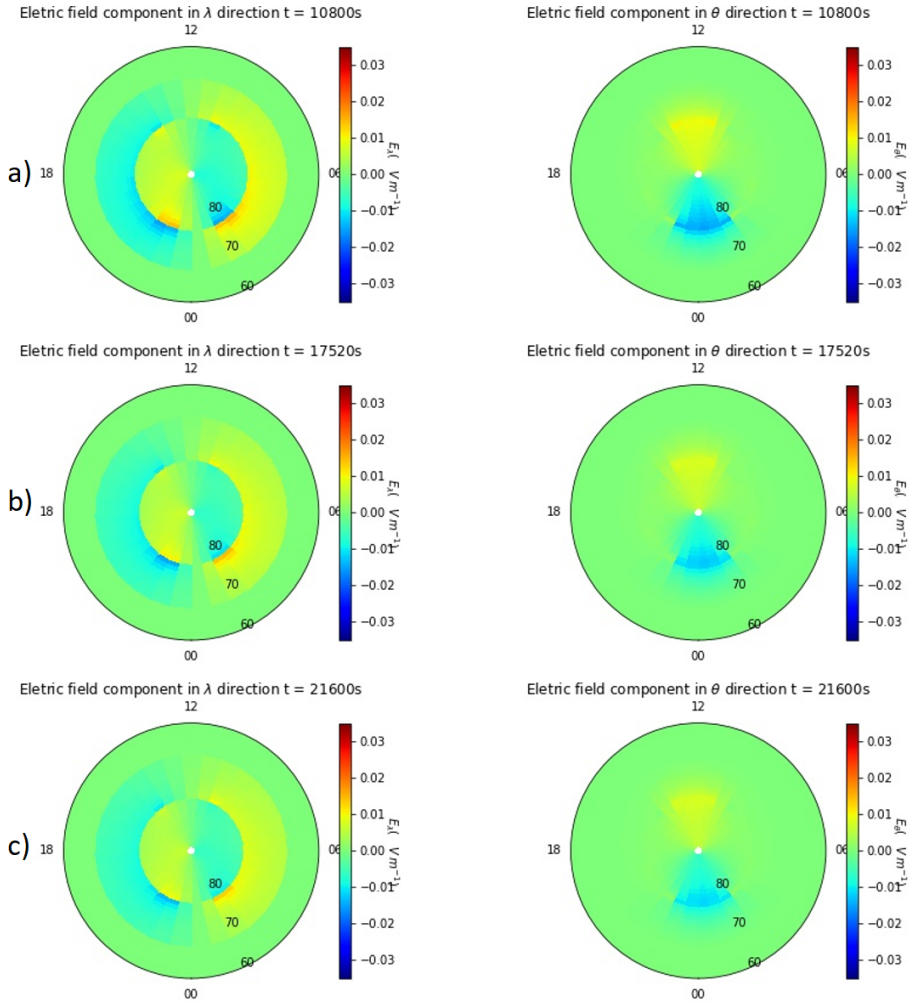


Figure 4.14: The calculated electric field components for $\lambda$ and $\theta$. For all three events we observe somewhat low values, but it as expected as all three events takes place during a weak IMF.

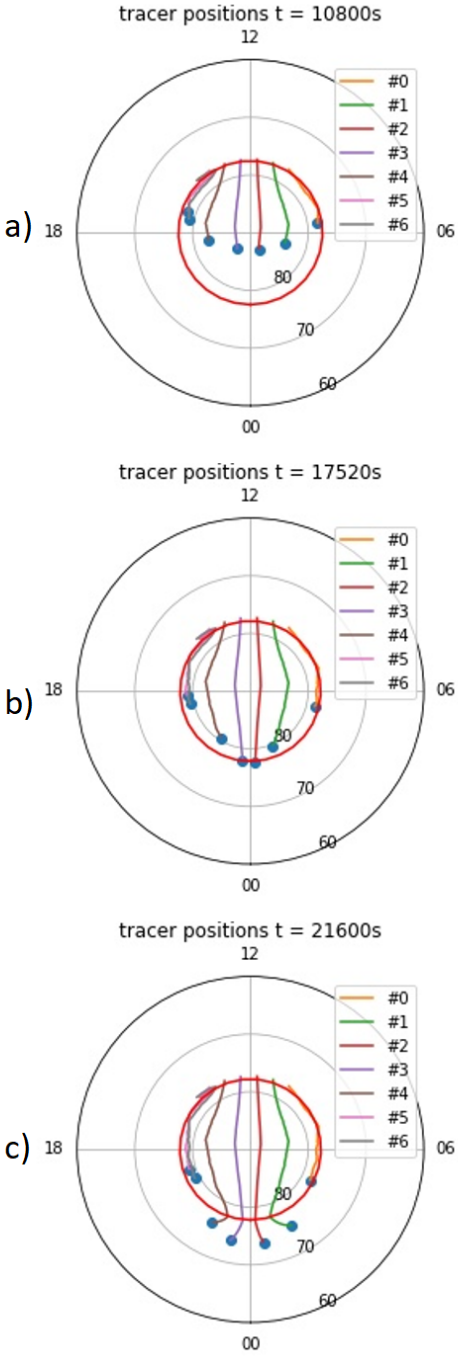


Figure 4.15: Tracer paths allowing us to see the current position of each tracer for each snapshot and also the path they have travelled. We are finally able to observe the first tracer particle, #2, that has reached the nightside OCB in event *b*. The OCB is marked by the red line.

By the end of the time series the tracer particles have finally reached the nightside OCB, but they did not arrive until an hour later than expected, so we again look at the mean velocities of each tracer particle. In Table 4.5 we observe values that are somewhere between those of Case B and D.

Table 4.5: Calculated mean velocity of each tracer particle placed along the OCB. The IMF intervals in use are, in order, [4.03, 37.70)nT [-39.00, -4.03)nT [-0.02, 0.69)nT [-0.73, -0.02)nT. Starting position for tracer #0 is at 10MLT while tracer #6 starts at 15MLT.

| Tracer # | Mean velocity [m/s] |
|---|---|
| 0 | 97.6 |
| 1 | 148.6 |
| 2 | 149.1 |
| 3 | 149.5 |
| 4 | 143.9 |
| 5 | 116.5 |
| 6 | 114.8 |

## 4.6 Case F: IMF Z interval -0.5nT turning to 0.5nT with an offset to the generated values

The relatively low values for the mean velocities in case B, C, D and E are the reasoning for these next two cases. We add an offset of 50kV to both day- and nightside reconnection for two of the time series, that of case B and D.

Figure 4.16 is similar to Figure 4.4, the only difference being an offset where 50kV is added to the mean value of the reconnection rates. The polar cap flux stays unchanged since equation 3.7 is dependent on the difference in reconnection rates and not the individual values. We study the "same" events as in case B, as to compare how these events differ with an offset. The three events are *a,b* and *c* that represent 3360s (00:56 UT), 6120s (01:42 UT) and 10320s (02:52 UT).

Figure 4.17 display electric fields the same events case B, but it is now much harder to distinguish whether there is mainly day- or nightside reconnection. Event *a* in Case B had mainly nightside activity and *c* mainly had activity on the dayside, seen in Figure 4.5. In the events in Figure 4.17 this is not prominent due to intensity bar not being set to an appropriate scale and the now large values for the reconnection rates. What we now observe are values for the electric field components that are in the are of 50mV/m and -50mV/m.

Figure 4.18 display different tracer particle behaviour as opposed to the tracer particles in case B, before event *b* the tracers had already passed the nightside OCB and by the

last snapshot the tracer particles had started to travel along the return flow region towards the dayside. The first tracer would arrive after only 5400s (01:30 UT) and the last would arrive after 8520s (02:22 UT).

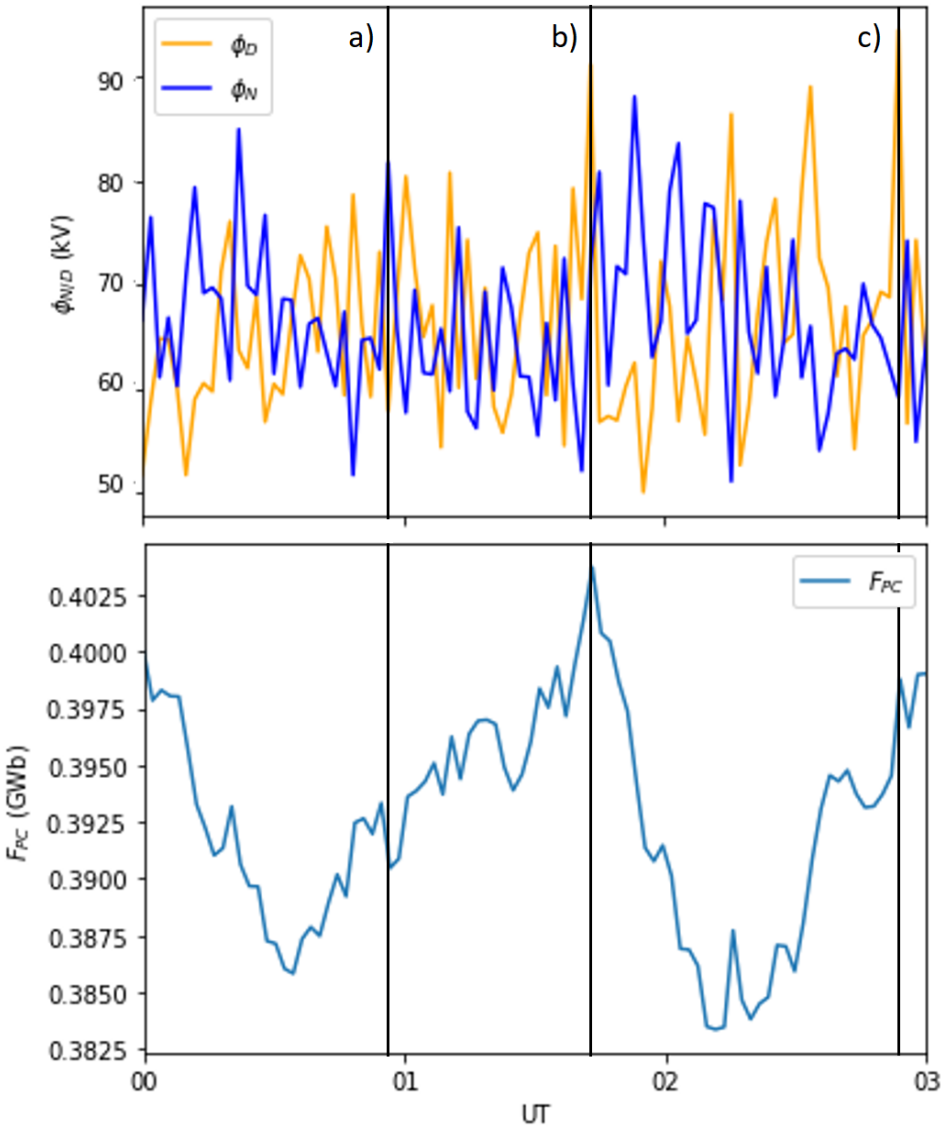


Figure 4.16: Generated reconnection rates ($\Phi_{D/N}$), this case is similar to Case A with the same snapshots, but the reconnection rates have an added offset of 50kV. This leads to larger values for the same timed snapshots, but we still observe the same values for the polar cap flux.

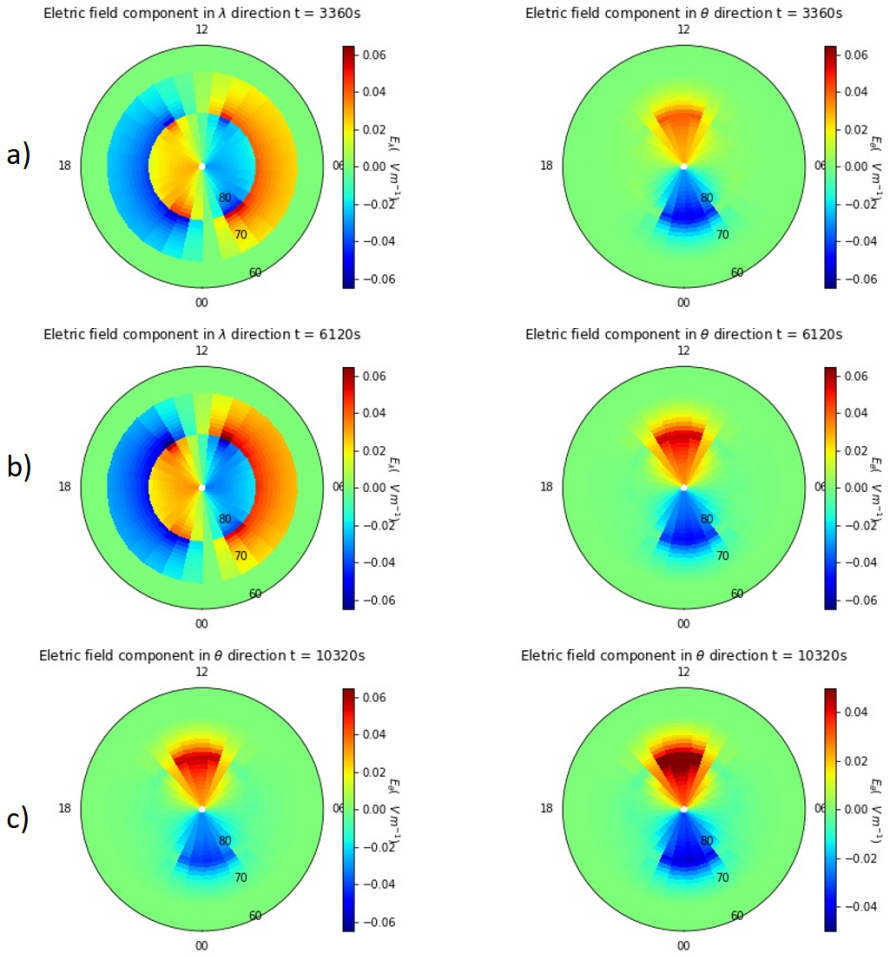


Figure 4.17: The calculated electric field components for $\lambda$ and $\theta$, but now the values are larger and range from 50mV/m and -50mV/m. In event $a$ to $b$ we observe a slight expansion before a slight contraction in event $b$ to $c$.

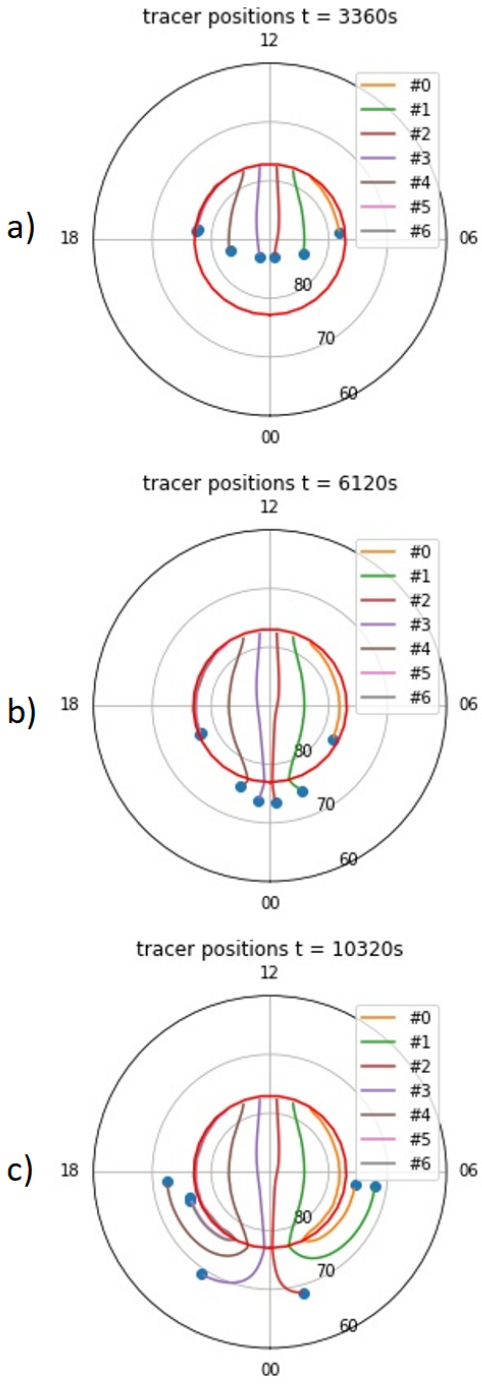


Figure 4.18: Tracer paths allowing us to see the current position of each tracer for each snapshot and also the path they have travelled. Unlike Case B, which use the same time series, the tracer particles have now reached the nightside OCB prior to event *b*.The OCB is marked by the red line.

We will later want to compare the mean velocities between Case B and Case F, and the values for Case F are tabulated in Table 4.6. In this table we observe that the values are significantly larger than any of the previous events and that is verified by the relatively early arrival to the nightside OCB, viewed in figure 4.18c.

Table 4.6: Calculated mean velocity of each tracer particle placed along the OCB. The time series studied is the same as in Case B, but with an offset of 50kV to the reconnection rates. Starting position for tracer #0 is at 10MLT while tracer #6 starts at 15MLT.

| Tracer # | Mean velocity [m/s] |
|---|---|
| 0 | 365.0 |
| 1 | 492.7 |
| 2 | 528.3 |
| 3 | 524.6 |
| 4 | 478.1 |
| 5 | 340.5 |
| 6 | 327.1 |

## 4.7 Case G: IMF Z interval -5.0nT turning to 5.0nT with an offset to the generated values

Figure 4.19 showcase the same time series as in case D, just with an offset of 50kV just like in case F. The reconnection rates are again similar, but now has values up to 120kV compared to the maximum of 70kV in case D. Again the polar cap flux is unchanged due to the difference in the reconnection rates being the main parameter in equation 3.7. We study the same snapshots that we studied in case D, 3120s (00:52 UT), 5400s (01:30 UT) and 10080s (02:48 UT).

Figure 4.20 are electric field components similar to that displayed in Figure 4.11. Whether the day- or nightside has the most activity is not clear in this figure either, compared to Figure 4.17, and also has rather lage values in the interval of 65mV/m and -65mV/m.

In Figure 4.21 we observe similar behaviour for particle #6 to that of particle #6 in case D. And similar to case F the tracers do reach the nightside OCB by event *b*. By event *c* the tracer particles has started returning through the return flow region, just like in Figure 4.3 and Figure 4.18. ere we observe our fastest tracers, arriving as early as 4920s (01:22 UT) and the latest tracers would arrive after 9120s (02:32 UT). The latter being tje tracing taking a detour through the dayside return flow region.

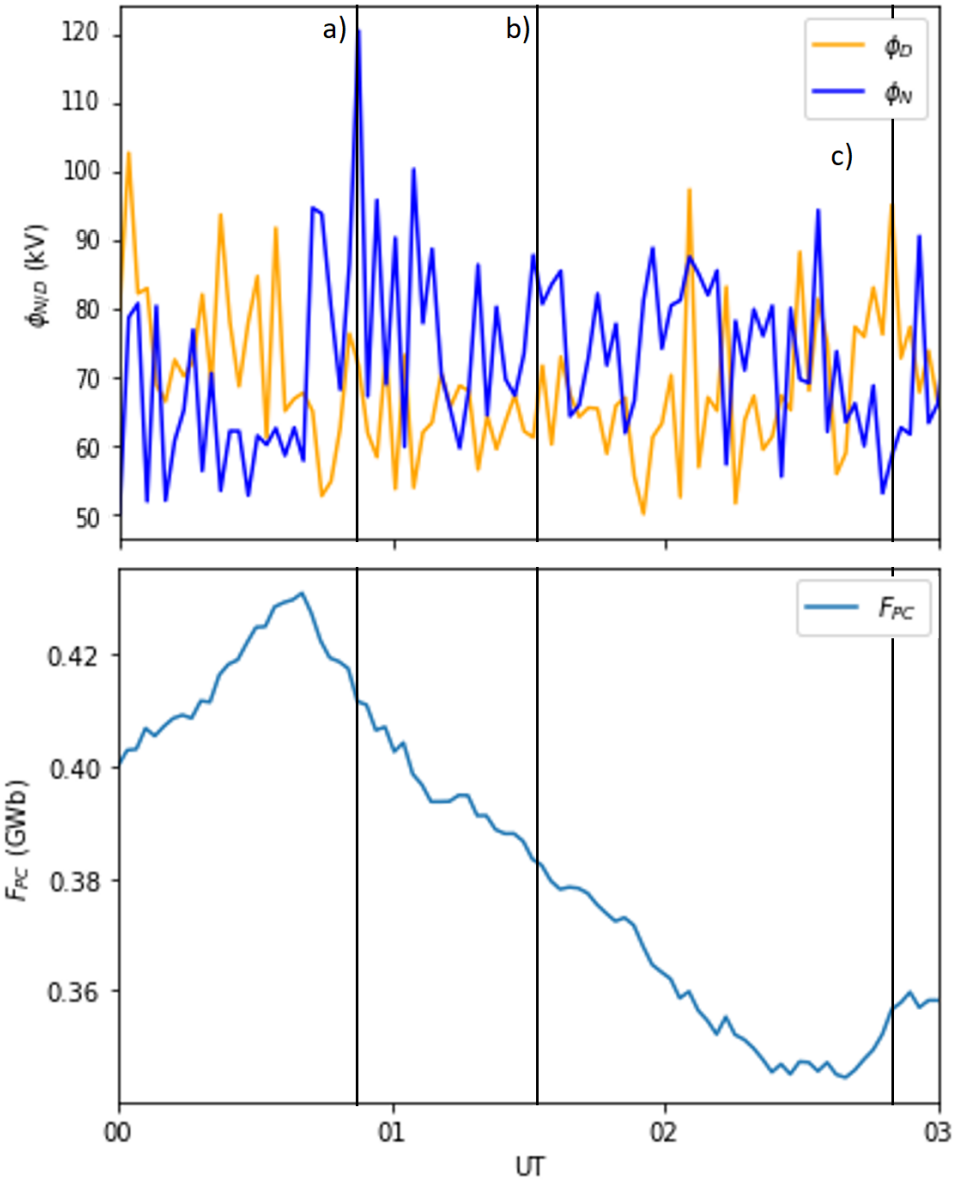


Figure 4.19: Generated reconnection rates ($\Phi_{D/N}$). Again the reconnection rates are similar to that of the parallel case, case D, but has a 50kV offset. Polar cap flux ($F_{pc}$) with initial value 0.4GWb still varies identical to its parallel case.

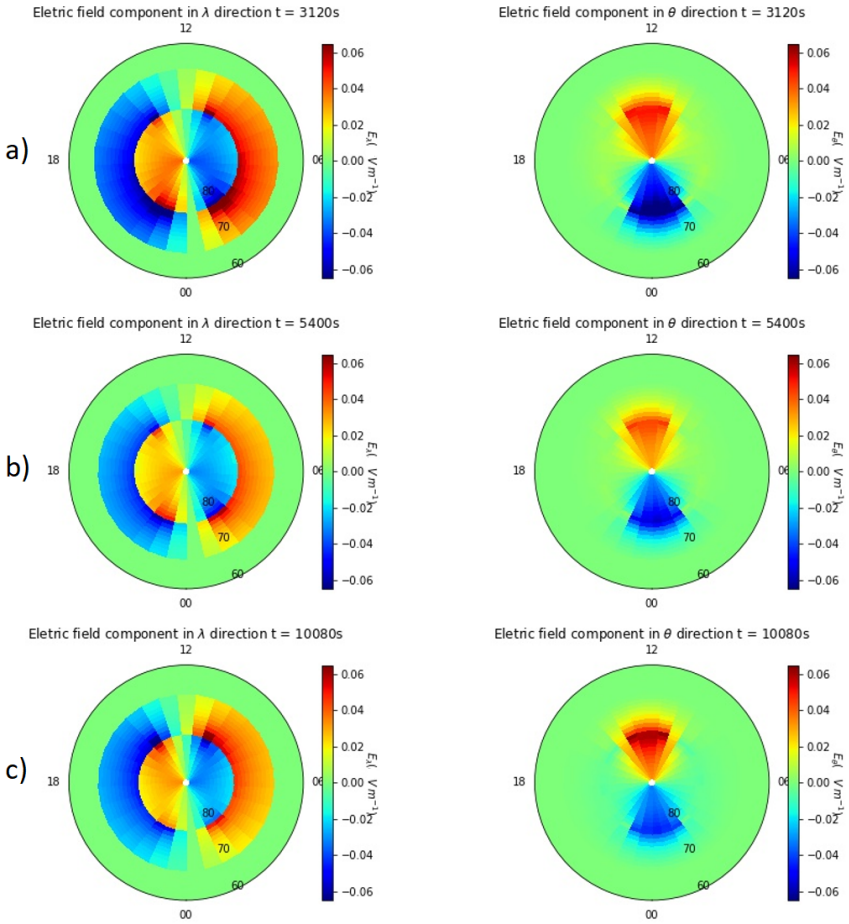


Figure 4.20: The calculated electric field components for $\lambda$ and $\theta$, the values are again a lot larger than that of the parallel case and it is hard to distinguish between dominating dayside or nightside activity.

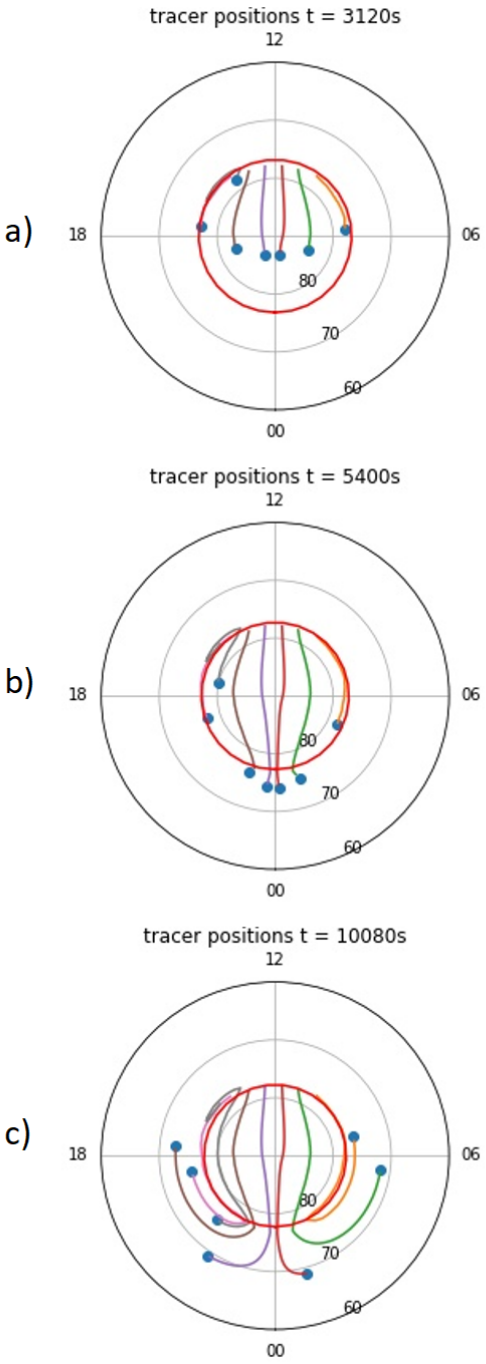


Figure 4.21: Tracer paths allowing us to see the current position of each tracer for each snapshot and also the path they have travelled. By the last snapshot we see clear twin-cell patterns created by all of the tracer particles. The OCB is marked by the red line.

We tabulate the calculated mean velocities in Table 4.7. These values are the highest calculated values of all cases.

Table 4.7: Calculated mean velocity of each tracer particle placed along the OCB. The time series studied is the same as in Case D, but with an offset of 50kV to the reconnection rates. Starting position for tracer #0 is at 10MLT while tracer #6 starts at 15MLT.

| Tracer # | Mean velocity [m/s] |
|---|---|
| 0 | 412.6 |
| 1 | 546.4 |
| 2 | 584.2 |
| 3 | 580.2 |
| 4 | 526.0 |
| 5 | 380.7 |
| 6 | 482.8 |

## 4.8 Propagation time distribution

We observe that the reconnection rates used for cases A, F and G all has tracers that arrive at the nightside OCB within the span of the 3 hours. To study how a polar cap patch propagates in these cases, across the northern hemisphere, we use our model for 1000 tracers that has starting positions evenly spaced between the longitudes 09MLT and 15MLT. These MLT values correspond to where we expect to find dayside reservoirs of high-density plasma (Follestad et al., 2019). We store the travel time of each tracer particle and the distributions are presented in figures 4.22.

In Figure 4.22 we can see the travel time distribution for Case A, where we study the ECPC model for a reconnection time series similar to that of Milan (2013). We observe a distribution reminiscence of a gamma distribution. In the same figure we also see the travel time distribution for cases F an G, here we also observe distributionts that are remeniscent of a gamma distribution. Here we observe that the tracers of Case F generally arrive at the nightside OCB later than those of Case G, which do make sense due to the latter being a strong IMF and for their parallel cases the latter also had higher mean velocities. While Case A has been corrected for the delayed start of the tracers, reconnection rates were set to 0 the first 40minutes, but they still arrive a lot later. The largest mean velocity, of the seven tracers originally studied, in Case A would reach about 400m/s, this is only 80% of a mean velocity of 500m/s tat we would observe for the other cases. The fastest tracer would reach the nightside OCB at 7800s (02:10 UT), 5400s (01:30 UT) and 4920s (01:22 UT) for cases A, F and G respectively. While the last tracers would reach the nightside OCB after 9960s (02:46 UT), 8520s (02:22 UT) and 9120s (02:32 UT) in the same order.

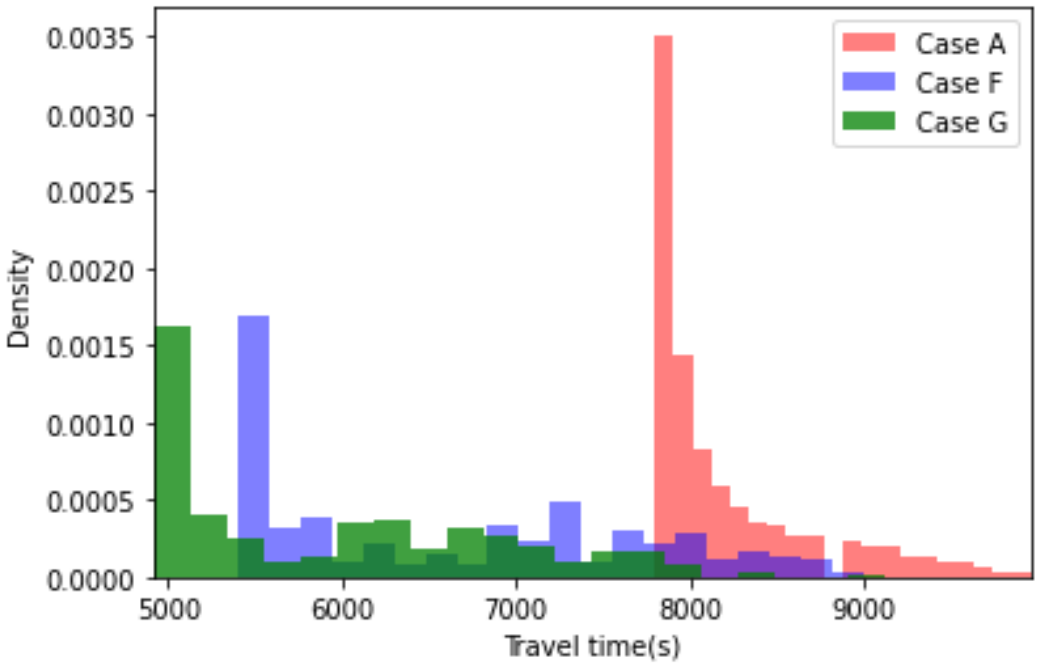


Figure 4.22: Distribution of arrival times for Cases A, F and G. The fastest tracers reaches the nightside OCB approximately 2160s, 35min, in Case A. For both cases F and G the fastest tracer would arrive 3360s, 56 minutes, prior to the slowest tracers. Common for all cases are that the tracers who arrived the earliest are also the ones with higher density.

Comaring the distributions is hard due to the big difference in propagation time. In Figure 4.23 we see the distributions of tracer arrivals at the nightside OCB relative to the first arrving tracer. So that 120s is 2 minutes after the first tracer has arrived.

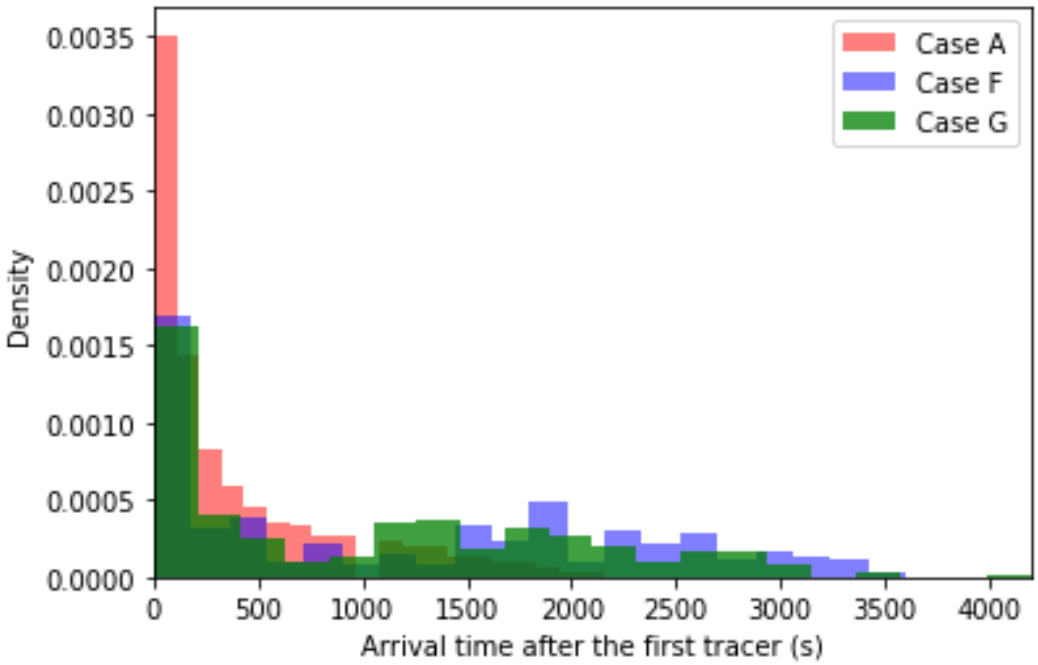


Figure 4.23: Distribution of arrival times after the first tracer has exited the nightside polar cap

# Chapter 5

# Discussion

We have been able to portray the main features of the ECPC model with the generated reconnection rates, the model does expand for dominating dayside reconnection and contract for dominating nightside reconnection. This helps govern the location of the OCB and the electric field helps propagate our tracer particles forward, towards the nightside OCB. In the following sections we will expand on the results presented for the seven case studies. Each case study produced a polar cap flux, electric fields and tracer particle propagation that would evolve parallel to the reconnection rates.

## 5.1 Predicted convection and real life cases

The ECPC model is a convection model, and it predict twin-cell patterns. This convection pattern also occur during the Dungey cycle. Comparing this convection pattern with that of the convection maps of the Super Dual Auroral Radar Network (SuperDARN) reveals that this may not be the most accurate representation of a convection pattern. SuperDARN is a network of 30 high-frequency radars located from mid latitudes and all the way to the polar regions, as stated in the SuperDARN website. Its primary objective is to map high-latitude plasma convection. In Figure 5.1 we see a convection map, retrieved from the SuperDARN website. The date is 14th March 2015 and the snapshot is taken at 20:00UT. We observe the two cells in the twin-cell convection pattern as red and blue areas. They do resemble a twin-cell, but there is no perfect symmetry along the noon-midnight axis nor the dawn-dusk axis.

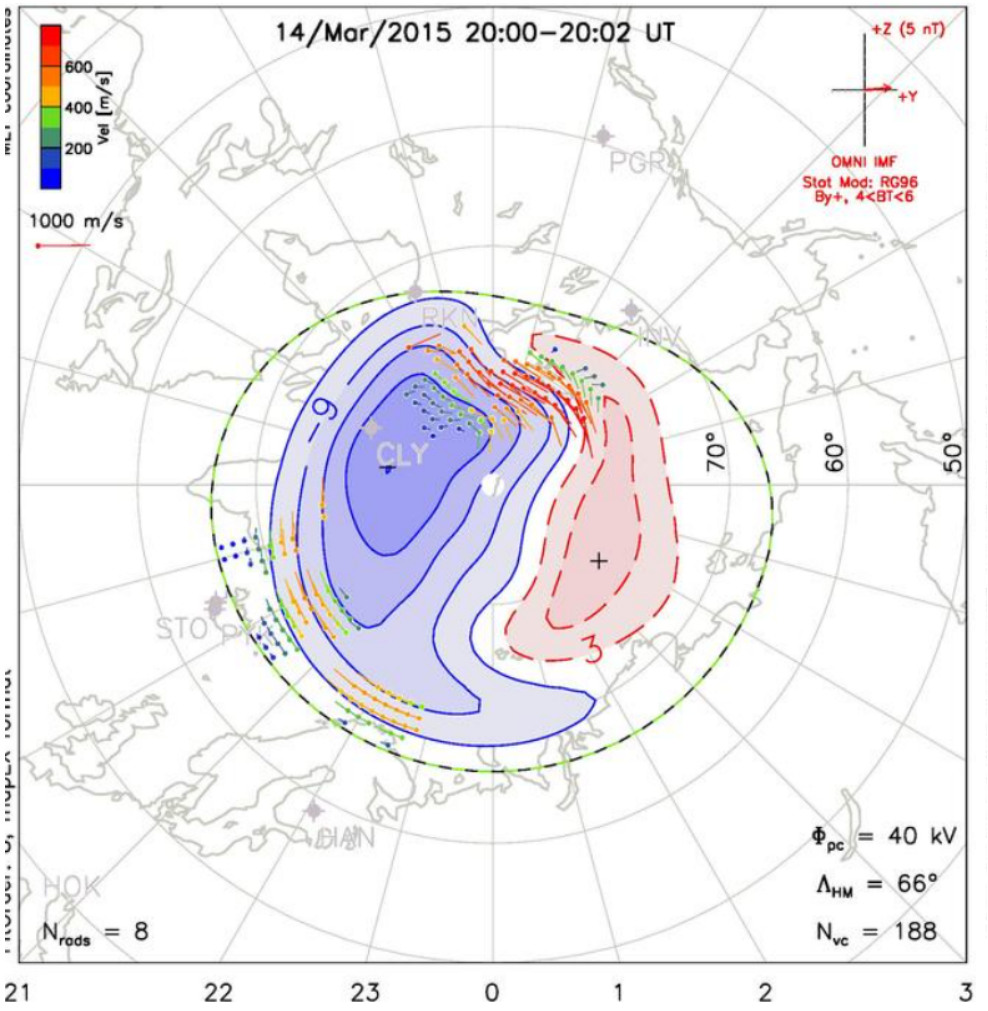


Figure 5.1: In this figure we see a convection map from the 14th March 2015 20:00UT from the northern hemisphere. The cells are apparent, but we do not observe that good of a symmetry as predicted by the ECPC paradigm. Retrieved from the SuperDARN website.

The lack of perfect twin-cell patten in Figure 5.1 is only one case. The convection pattern predicted by ECPC is really a statistical average of convection patterns and if we studied more cases through the use of the convection maps of SuperDARN we should be able to see an even more prominent twin-cell convection pattern. It is also shown in a case study by Follestad et al. (2019) the ECPC would predict the

nightside arrival of a plasma patch with a 5 min accuracy, despite there not being perfect a twin-cell convection pattern.

## 5.2 Polar cap flux, electric fields and mean velocities

Our ECPC model was able to reproduce the polar cap flux and the electric fields from Milan (2013), this was used as a proof of concept before further testing of the model for different reconnection rate time series. The expansion and contraction were more prominent between the labelled events in Case A as opposed the six latter case studies. This is due to the larger change in polar cup flux. For case A the polar cap flux would almost double and the be reduced beyond its initial value. While cases B, C, D, E, F and G all had changes in their polar cap flux they where of a smaller scale. The expanding and contracting is still in the model for the latter cases, but not as prominent.

The reconnection rates of Case A produce electric field values up to 35mV/m, this give the tracers velocities around 500m/s, these values are reasonable (Fukui, Buchau & Valladares, 1994). Fukui et al. (1994) would observe varying drift velocities for polar cap patches ranging down to 100m/s, but not often. The range 350-500m/s was more commonly observed. Patches are believed to move across the polar cap with typical velocities of 300-1000m/s (Weber et al., 1984). Our cases B and C has only produces velocities half of that. It is clear that this is not enough to perform a case study where we study the propagation time within a timespan of 3 hours, as seen by the tracer paths in figures and . Case D is similar in that it does produce velocities that are similar to that of Case A, but that only applies for a few time steps and this is clear from the mean velocities and we again observe mean velocities that are nowhere near that of the 350-500m/s range.

We did confirm the the tracers will eventually reach the nightside through the study of Case E. We would observe the first tracer to reach the nightside OCB after nearly 5 hours of polar cap patch propagation, this is a lot slower than what is expected. Predicted propagation times varies from 2-3 hours (Oksavik et al., 2010), and an open flux tube is generally believed to travel for 2-4 hours from the dayside to the nightside OCB (Lockwood, Cowley & Freeman, 1990). This propagation time and mean velocities not being any larger than 149m/s is enough for us to deem this case study unfit for estimating polar cap patch propagation time as a part of a larger space weather forecasting model.

The cases F and G produce rather large values for the electric fields, compared to all previous cases, and in turn they produce the largest velocities. With the either reconnection rate being at least 50kV we could expect high electric field activity at both day- and nightside at all times. Reconnection, on either sides, are driving for large-scale ionospheric convection (Lockwood et al., 1990; Lockwood & Cowley, 1992).

This was the motivation for wanting to introduce an offset, an increased strength in the plasma convection. The observed mean velocities fall in the range of 350-500m/s, coinciding with studies by Weber et al. (1984). We proceed the case studies for cases A, F and G as their velocities and propagation times have better coherence with what has been observed previously.

## 5.3 Tracer paths and propagation time distribution

When studying the propagation of these tracer particles we observe a path that clearly follow a twin-cell convection pattern, close to an ideal twin cell pattern, but in Case F and G some did not. Some would travel antisunwards across the polar cap before suddenly passing trough the dayside return flow region. Earlier we claimed this to be due a rapid decrease in the polar cap flux, causing the OCB to pulse past the particle. This is, according to the equation 3.9 used to calculate the rate of polar cap flux, only possible when the nightside reconnection rate is substantially larger than that of the dayside. This may be due to the our generated reconnection rates. The rates we use are a mean of 10 samples and this is not large enough to avoid any outlying values to cause weird interactions, so the odd behaving tracers were not included when calculating the propagation time distribution and to take further actions we could have smoothed out the reconnection rates through least square fitting.

Further on, the ECPC model symmetry for the convection patterns along the noon-midnight axis and the dusk-dawn axis. This implies that a tracer starting at 12MLT would propagate across the polar cap and arrive at 00MLT or that a tracer starting prior to noon will arrive past midnight. In reality there may be asymmetry along the aforementioned axis and a tracer starting at noon is not predetermined to arrive at midnight (Pettigrew, Shepherd & Ruohoniemi, 2010). It also assumes that the tracers propagate in a steady state manner, in a study by Oksavik et at. (2010) flow speeds were observed to be more dynamic and pulsed.

Our tracer paths are only affected by the E×B-drift and the expansion and contraction introduced through the ECPC model. Realistically a patch crossing the polar cap would also be affected by change in shape of the convection pattern (Crowley et al., 2000). As shown by Crowley et al. (2000) the patch can change as it follows the varying convection pattern. This could lead to our tracers no longer following a predictable twin-cell convection pattern and it would increase the uncertainty in predicting the MLT location where a patch would exit the nightside OCB.

The ECPC model also neglects smaller phenomena such as flow channels. Flow channels are small regions (100-200km wide) that accelerate drift velocities 1000-4000m/s and are associated with dayside reconnection (Pinnock et al., 1993; Nishimura et al., 2014). They appear at high latitudes, not too far from the cusp (Oksavik, Moen & Carlson, 2004; Moen et al., 2008).This could reduce propagation time and this is not

included in the model. Given that these channels are of the size 100km the increase in velocity would maybe decrease propagation time by 10minutes per interaction, assuming a mean velocity of 400m/s. Tough this would decrease travel time for all cases that would decrease the drift velocities of Case F and G and they are already rather large considering their short propagation times. This would make it hard to compare our values to previous studies. On the other hand introducing the flow channels to the model could change the distribution, reducing propagation time for some tracers.

We do see from cases F and G that we may have propagation times that borderline to unrealistically fast, but comparing with Case A, the distributions seem good. Due to the symmetry in the model a tracer starting at 11MLT would propagate for the same amount of time as a tracer starting at 13MLT and so on. For Case A a tracer starting at 12MLT would propagate for 7800s (02:10UT) while a tracer starting at 11MLT or 13MLT would propagate for only 2 minutes longer. A tracer starting at 10.5MLT or 13.5MLT would propagate for 7 minutes longer than that of the 12MLT tracer. For the two cases F and G there are similar observations. F has a 4 minute delay between 12MLT and 11MLT, but the tracer at 10.5MLT would reach the nightside OCB 4 minutes prior to that of the 12MLT. It is unsure as to why. For Case G a tracer at 11MLT, 12MLT and 13MLT would all propagate for the same amount of time while a tracer starting at 10.5MLT would propagate for 6 minutes.If we move to tracers that start at 15MLT and 09MLT we would observe tracers that propagated for 24-26 minutes longer than of those starting at noon. Patches are usually on the magnitude 1000km in size in the dawn-dusk direction (MacDougall & Jayachandran, 2007), and this is the equivalent of about 10° and in the a study by Follestad et al.(2019) a patch covering about 20° was studied. 01MLT is about 15°, so patches that propagate from close to noon could be predicted with good accuracy. Some odd observations are that of the propagation times for 12.5MLT, 11.5MLT, 14.5 and 09.5MLT. The two first starting MLTs would give the shortest propagation times while the two latter would give the longest propagation times, this was common for all cases. The ones that were faster would propagate 2-6 minutes faster than the noon tracers while the slower would propagate up to 28 minutes slower. It is unclear as to what the reasoning is, but there is some clear symmetry there. Again, the tracers that start closer to noon are not too far off the other propagation times while the ones closer to dawn/dusk varies a lot more.

The propagation time in this model is also dependent on the OCB location. Case A would have the largest changes in OCB location due to its larger changes in polar cap flux, the location of the OCB would vary between co-latitude 17° and 12°, a 5° difference this is about a 500km difference and assuming a mean velocity of 400m/s, depending on expansion or contraction this would add or subtract up to 20 minutes of propagation time for some tracers. The maximum expansion and contraction would take place more tan an our apart, and the tracers would keep up with constant change in OCB location in this case and this uncertainty should is not too large.

Our hypothesis was that the ECPC model could predict patch propagation across

the polar cap and predict the arrival of the patch at the nightside OCB. Some inner dynamics that have been neglected by the model, may affect the accuracy in predicting propagation time and exact behaviour. This includes a varying convection pattern and flow channels. The first would allow us to study exact tracer paths while the latter being able to introduce velocities much larger than what is predicted by ECPC. Flow channels happen on smaller scales and therefore do not last for a significant amount of time, reducing propagation times by some minutes and mainly affect the distribution rather than the credibility of the prediction model. The varying convection pattern could be of more concern as it makes it harder to predict location and timing of scintillations, but a change in some few degrees for a plasma blob is not too significant since the satellite signal only has to pass through the patch and if these blobs are wide enough then it won make a difference if it exits at 00MLT or 23MLT. What the model does well is mimicking typical behaviour for sub storms, through decoupling of day- and nightside reconnection and emulate the growth phase and expansion phase respectively (Lockwood & Cowley, 1992). The latter allowing for patches to exit the polar cap. Patches exiting there, forming blobs, lead to the most significant disturbances in GNSS recievers (Moen et al., 2013; Jin et al., 2014). The ability to model the excitation is rather unique and would make a great basis for a space weather forecasting model.

# Chapter 6

# Conclusion

We have shown that the ECPC model could be used to predict polar cap patch propagation towards the nightside OCB. When introducing rather large reconnection rates, with offsets, that introduced large velocities the model would produce patch propagation that also would borderline even shorter. It would also produce slow propagation times when the reconnection rates would be of lower values and when introduced to a time series that had previously been used as a proof of concept it would show behaviour expected of a polar cap patch through its convection pattern, expanding/contracting polar cap and propagation times. Tough the results did not display a complete picture of the inner dynamics of a polar cap, neglecting variations in convection pattern and flow channels, the propagation times were still realistic compared to previous studies (Oksavik et al., 2010). A study of the propagation time densities would reveal that the propagation time of patches starting closer to noon could be predicted with a relatively small uncertainty where as patches starting closer to dawn/dusk are harder to predict as patch width leads to a larger uncertainty. From the observation of these studies, the ECPC model as a prediction model would see more fit for patches detected closer to noon. As suggested by Follestad et al. (2019) a space weather forecasting model would benefit from a patch detecting system, such could be achieved through the use of satellites carrying Langmuir Probes (Spicher et al., 2017).

Our use of small sample sizes may lead to larger uncertainties in the dawn/dusk regions, so it may be advised to repeat these case studies with the larger sample sizes for the reconnection rates and better handling of the time series. This may produce distributions that are easier to study and more accurate when compared with previous studies on polar cap patch propagations.

# Chapter 7

# Outlook

Only three out of seven case studies could be used to study the propagation times of polar cap patches, but there are many different reconnection rate time series that can be applied to the ECPC model. We would use a mean of 10 different time series, generated from the same IMF interval, and run the model for 1000 different starting locations for the tracer. This is just one of many ways to test the ECPC as a basis for space weather forecast. One could for example have try to run each time series separately and track one tracer, starting at the same location, for each of those 10 time series. There is also a possibility to do as done in cases F and G, introduce an offset to the time series, but use different offsets. A third option is to do like Follestad et al. (2019) use SuperDARN, calculate the dayside- and nightside reconnection rate, assuming that the SuperDARN measured cross polar cap potential is the average of those two. That way one can compare the accuracy of the ECPC to several real life cases. The goal would be to perform enough case studies so that one would have a good statistical model describing the abilities of the ECPC to accurately predict patch propagation.

# References


Allen, J., Sauer, H., Frank, L. & Reiff, P. (1989). Effects of the march 1989 solar activity. *Eos, Transactions American Geophysical Union*, *70*(46), 1479–1488.

Axford, W. (1964). Viscous interaction between the solar wind and the earth's magnetosphere. *Planetary and Space Science*, *12*(1), 45–53.

Bruntz, R., Lopez, R., Wiltberger, M. & Lyon, J. (2012). Investigation of the viscous potential using an mhd simulation. *Journal of Geophysical Research: Space Physics*, *117*(A3).

Cowley, S. & Lockwood, M. (1992). Excitation and decay of solar wind-driven flows in the magnetosphere-ionosphere system. In *Annales geophysicae* (Vol. 10, pp. 103–115).

Crowley, G., Ridley, A., Deist, D., Wing, S., Knipp, D., Emery, B., ... Reinisch, B. (2000). Transformation of high-latitude ionospheric f region patches into blobs during the march 21, 1990, storm. *Journal of Geophysical Research: Space Physics*, *105*(A3), 5215–5230.

Eroshenko, E., Belov, A., Boteler, D., Gaidash, S., Lobkov, S., Pirjola, R. & Trichtchenko, L. (2010). Effects of strong geomagnetic storms on northern railways in russia. *Advances in space research*, *46*(9), 1102–1110.

Follestad, A. F., Clausen, L. B. N., Thomas, E. G., Jin, Y. & Coster, A. (2019). Polar cap patch prediction in the expanding contracting polar cap paradigm. *AGU Journals*. Retrieved from https://agupubs.onlinelibrary.wiley.com/doi/10.1029/2019SW002276

Freeman, M. (2003). A unified model of the response of ionospheric convection to changes in the interplanetary magnetic field. *Journal of Geophysical Research: Space Physics*, *108*(A1), SMP–14.

Freeman, M. & Southwood, D. (1988). The effect of magnetospheric erosion on mid-and high-latitude ionospheric flows. *Planetary and space science*, *36*(5), 509–522.

Fukui, K., Buchau, J. & Valladares, C. (1994). Convection of polar cap patches observed at qaanaaq, greenland during the winter of 1989–1990. *Radio science*, *29*(01), 231–248.

Garner, T., Harris, R., York, J., Herbster, C., Minter III, C. & Hampton, D. (2011).

An auroral scintillation observation using precise, collocated gps receivers. *Radio Science*, *46*(01), 1–11.

Hey, J., Parsons, S. & Phillips, J. (1946). Fluctuations in cosmic radiation at radio-frequencies. *Nature*, *158*(4007), 234–234.

Jacobsen, K. S. & Andalsvik, Y. L. (2016). Overview of the 2015 st. patrick's day storm and its consequences for rtk and ppp positioning in norway. *Journal of Space Weather and Space Climate*, *6*, A9.

Jakowski, N., Stankov, S. & Klaehn, D. (2005). Operational space weather service for gnss precise positioning. In *Annales geophysicae* (Vol. 23, pp. 3071–3079).

Jakowski, N., Wilken, V., Schlueter, S., Stankov, S. & Heise, S. (2005). Ionospheric space weather effects monitored by simultaneous ground and space based gnss signals. *Journal of atmospheric and solar-terrestrial physics*, *67*(12), 1074–1084.

Jin, Y., Moen, J. I. & Miloch, W. J. (2014). Gps scintillation effects associated with polar cap patches and substorm auroral activity: Direct comparison. *Journal of Space Weather and Space Climate*, *4*, A23.

Kintner, P. M., Ledvina, B. M. & De Paula, E. (2007). Gps and ionospheric scintillations. *Space weather*, *5*(9).

Lockwood, M. & Carlson Jr, H. (1992). Production of polar cap electron density patches by transient magnetopause reconnection. *Geophysical research letters*, *19*(17), 1731–1734.

Lockwood, M. & Cowley, S. (1992). Ionospheric convection and the substorm cycle.

Lockwood, M., Cowley, S. & Freeman, M. (1990). The excitation of plasma convection in the high-latitude ionosphere. *Journal of Geophysical Research: Space Physics*, *95*(A6), 7961–7972.

MacDougall, J. & Jayachandran, P. (2007). Polar patches: Auroral zone precipitation effects. *Journal of Geophysical Research: Space Physics*, *112*(A5).

McCaffrey, A. & Jayachandran, P. (2019). Determination of the refractive contribution to gps phase "scintillation". *Journal of Geophysical Research: Space Physics*, *124*(2), 1454–1469.

Milan, S., Gosling, J. & Hubert, B. (2012). Relationship between interplanetary parameters and the magnetopause reconnection rate quantified from observations of the expanding polar cap. *Journal of Geophysical Research: Space Physics*, *117*(A3).

Milan, S., Lester, M., Greenwald, R. & Sofko, G. (1999). The ionospheric signature of transient dayside reconnection and the associated pulsed convection return flow. In *Annales geophysicae* (Vol. 17, pp. 1166–1171).

Milan, S., Provan, G. & Hubert, B. (2007). Magnetic flux transport in the dungey cycle: A survey of dayside and nightside reconnection rates. *Journal of Geophysical Research: Space Physics*, *112*(A1).

Milan, S. E. (2013). Modeling birkeland currents in the expanding/contracting polar cap paradigm. *Journal of Geophysical Research: Space Physics*, *118*(9), 5532–5542.

Moen, J., Carlson, H., Oksavik, K., Nielsen, C., Pryse, S., Middleton, H., ... Gallop, P. (2006). Eiscat observations of plasma patches at sub-auroral cusp latitudes. In *Annales geophysicae* (Vol. 24, pp. 2363–2374).

Moen, J., Oksavik, K., Alfonsi, L., Daabakk, Y., Romano, V. & Spogli, L. (2013). Space weather challenges of the polar cap ionosphere. *Journal of Space Weather and Space Climate*, *3*, A02.

Moen, J., Rinne, Y., Carlson, H., Oksavik, K., Fujii, R. & Opgenoorth, H. (2008). On the relationship between thin birkeland current arcs and reversed flow channels in the winter cusp/cleft ionosphere. *Journal of Geophysical Research: Space Physics*, *113*(A9).

Nagatsuma, T., Kataoka, R. & Kunitake, M. (2015). Estimating the solar wind conditions during an extreme geomagnetic storm: a case study of the event that occurred on march 13–14, 1989. *Earth, Planets and Space*, *67*(1), 1–10.

Nguyen, L. (2021). Modelling nigthside reconnection rates for the expanding/contracting polar cap paradigm.

Nishimura, Y., Lyons, L. R., Zou, Y., Oksavik, K., Moen, J., Clausen, L., ... others (2014). Day-night coupling by a localized flow channel visualized by polar cap patch propagation. *Geophysical Research Letters*, *41*(11), 3701–3709.

Oksavik, K., Barth, V., Moen, J. & Lester, M. (2010). On the entry and transit of high-density plasma across the polar cap. *Journal of Geophysical Research: Space Physics*, *115*(A12).

Oksavik, K., Moen, J. & Carlson, H. (2004). High-resolution observations of the small-scale flow pattern associated with a poleward moving auroral form in the cusp. *Geophysical Research Letters*, *31*(11).

Pécseli, H. L. (2013). *Waves and oscillations in plasmas*. CRC Press Boca Raton.

Pettigrew, E., Shepherd, S. & Ruohoniemi, J. (2010). Climatological patterns of high-latitude convection in the northern and southern hemispheres: Dipole tilt dependencies and interhemispheric comparisons. *Journal of Geophysical Research: Space Physics*, *115*(A7).

Pinnock, M., Rodger, A. S., Dudeney, J., Baker, K., Newell, P., Greenwald, R. & Greenspan, M. (1993). Observations of an enhanced convection channel in the cusp ionosphere. *Journal of Geophysical Research: Space Physics*, *98*(A3), 3767–3776.

Prölss, G. (2012). *Physics of the earth's space environment: an introduction*. Springer Science & Business Media.

Rostoker, G., Akasofu, S.-I., Foster, J., Greenwald, R., Kamide, Y., Kawasaki, K., ... Russell, C. (1980). Magnetospheric substorms—definition and signatures. *Journal of Geophysical Research: Space Physics*, *85*(A4), 1663–1668.

Russell, C. T., Luhmann, J. G. & Strangeway, R. J. (2016). *Space physics: An introduction*. Cambridge University Press.

Siscoe, G. & Huang, T. (1985). Polar cap inflation and deflation. *Journal of Geophysical Research: Space Physics*, *90*(A1), 543–547.

Spicher, A., Clausen, L. B. N., Miloch, W. J., Lofstad, V., Jin, Y. & Moen, J. I.

(2017). Interhemispheric study of polar cap patch occurrence based on swarm in situ data. *Journal of Geophysical Research: Space Physics*, *122*(3), 3837–3851.

Sreeja, V. (2016). Impact and mitigation of space weather effects on gnss receiver performance. *Geoscience Letters*, *3*(1), 1–13.

Weber, E. J., Buchau, J., Moore, J., Sharber, J., Livingston, R., Winningham, J. D. & Reinisch, B. (1984). F layer ionization patches in the polar cap. *Journal of Geophysical Research: Space Physics*, *89*(A3), 1683–1694.

Weber, E. J., Tsunoda, R. T., Buchau, J., Sheehan, R. E., Strickland, D. J., Whiting, W. & Moore, J. G. (1985). Coordinated measurements of auroral zone plasma enhancements. *Journal of Geophysical Research: Space Physics*, *90*(A7), 6497–6513.

Yeh, K. C. & Liu, C.-H. (1982). Radio wave scintillations in the ionosphere. *Proceedings of the IEEE*, *70*(4), 324–360.